nature communications

Article

https://doi.org/10.1038/s41467-024-52297-3

Entorhinal cortex vulnerability to human APP expression promotes hyperexcitability and tau pathology

Received: 26 October 2023

Accepted: 3 September 2024

Published online: 10 September 2024

Check for updates

Annie M. Goettemoeller[1,2], Emmie Banks[1,2], Prateek Kumar[3], Viktor J. Olah[1], Katharine E. McCann[4], Kelly South[1,2], Christina C. Ramelow[2,5], Anna Eaton[6], Duc M. Duong[5,8], Nicholas T. Seyfried[5,7,8], David Weinshenker[4], Srikant Rangaraju[3] ✉ & Matthew J. M. Rowan[1,8] ✉

Preventative treatment for Alzheimer's Disease (AD) is dire, yet mechanisms underlying early regional vulnerability remain unknown. In AD, one of the earliest pathophysiological correlates to cognitive decline is hyperexcitability, which is observed first in the entorhinal cortex. Why hyperexcitability preferentially emerges in specific regions in AD is unclear. Using regional, cell-type-specific proteomics and electrophysiology in wild-type mice, we uncovered a unique susceptibility of the entorhinal cortex to human amyloid precursor protein (hAPP). Entorhinal hyperexcitability resulted from selective vulnerability of parvalbumin (PV) interneurons, with respect to surrounding excitatory neurons. This effect was partially replicated with an APP chimera containing a humanized amyloid-beta sequence. EC hyperexcitability could be ameliorated by co-expression of human Tau with hAPP at the expense of increased pathological tau species, or by enhancing PV interneuron excitability in vivo. This study suggests early interventions targeting inhibitory neurons may protect vulnerable regions from the effects of APP/amyloid and tau pathology.

Alzheimer's Disease (AD) is the most prevalent neurodegenerative disease, yet current treatments are unable to prevent its initiation and progression. Although brain regions of early vulnerability have been known for over 30 years[1], our understanding of what makes certain areas more susceptible remains unknown. The first cortical region to display pathology and degeneration in AD is the Lateral Entorhinal Cortex (LEC)[1–4]. Notably, landmark studies identified Layer II (LII) neurons cells as highly vulnerable to early neurodegeneration with up to 60% cell death in mild AD patients and up to 90% in severe cases[2]. More recently, LII LEC principal neurons were also characterized as a cell population exhibiting amyloid pathology[4]. However, the distinctive features that impart vulnerability to neurons in the LEC AD remain unclear. Uncovering region-specific cellular mechanisms could improve our understanding of the initiating factors in the AD cascade and are imperative in determining potential interventions at a time when subsequent cognitive decline and neurodegeneration might still be prevented.

Here we show that the entorhinal cortex is more prone to hyperexcitability, with respect to the somatosensory cortex, following adult-onset expression of the human amyloid precursor protein (hAPP). Hyperexcitability is one of the earliest pathophysiological biomarkers in the human AD brain, and its emergence correlates with

[1]Department of Cell Biology, Emory University School of Medicine, Atlanta, GA, USA. [2]GDBBS Graduate Program, Laney Graduate School, Emory University, Atlanta, GA, USA. [3]Department of Neurology, Yale University, New Haven, CT, USA. [4]Department of Human Genetics, Emory University School of Medicine, Atlanta, GA, USA. [5]Department of Neurology, Emory University School of Medicine, Atlanta, GA, USA. [6]Department of Biomedical Engineering, Georgia Institute of Technology, Atlanta, GA, USA. [7]Department of Biochemistry, Emory University School of Medicine, Atlanta, GA, USA. [8]Center for Neurodegenerative Disease, Emory University School of Medicine, Atlanta, GA, USA. ✉e-mail: srikant.rangaraju@yale.edu; mjrowan@emory.edu

the severity of cognitive decline in individuals[5]. Hyperexcitability is also observed in recordings from in vivo and in vitro models of AD pathology[6–12], arising prior to amyloid plaque deposition[13] and likely contributing to spine degeneration[14]. Interestingly, hypermetabolism[15] and hyperexcitability[9,16] emerged in the LEC of a sporadic AD mouse model before spreading to other regions[3]. It was previously unclear whether cell-intrinsic changes in principal neuron excitability or other forms of circuit dysfunction are responsible for aberrant LEC activity following early APP/Aβ pathology. Hyperexcitability may arise due to changes in local circuit inhibition from GABAergic interneurons, with several lines of evidence demonstrating impaired inhibitory tone[6,9,15], most notably from fast-spiking parvalbumin+ (PV) interneurons[7,10,13]. Whether the basal properties of PV interneurons in the LEC confer functional vulnerability with respect to PV cells in other regions is unknown. Thus, here we observed baseline cellular and regional differences coupled with adult-onset, region-specific APP or Tau expression to dissect inherent vulnerabilities underlying susceptibility of the LEC to early AD pathology.

Results

PV interneurons in an AD-vulnerable region are functionally and molecularly distinct

We first compared active and passive features of excitatory neurons in AD-vulnerable and non-vulnerable cortical regions. Excitatory neurons in LII of Lateral Entorhinal Cortex (LEC) (highly vulnerable to early AD pathology[4]) and L5 pyramidal cells (PCs) in Somatosensory Cortex (SS Ctx) of wild type (WT) mice were chosen for comparison, as each represent projection output neurons and are innervated by similar dominant inhibitory networks[17]. Despite differences in their dendritic anatomy, axonal projections, and overall local circuit operations, these two cell types showed striking overlap in their firing capacity, AP waveforms, and most other biophysical features (Fig. 1a–c), with only slight biophysical differences noted (Supplementary Table 1). Because different cortical regions perform operations over non-overlapping frequency domains, we hypothesized that differences in the intrinsic excitability of inhibitory interneurons might help tune circuit activity locally. Thus, we assessed physiological phenotypes of 'fast-spiking' PV interneurons in each region, using an unbiased, PV-specific enhancer-AAV fluorescent targeting approach[18]. In the LEC, the E2 enhancer displayed high overlap (92.62 ± 5.7%) with PV+ somas from the previously established mouse model, PV-tdTom (Supplementary Fig. 7a, b). Surprisingly, PV interneurons in the LEC maximally fired at only half the rate of SS Ctx PV interneurons (Fig. 1d, e), likely due to their far broader action potentials with respect to PV interneurons recorded from SS Ctx (Fig. 1f–h)[17]. The first action potential of each AP train was also larger in amplitude in the LEC PV interneurons (Fig. 1f–h). Furthermore, resting membrane potential and AP threshold were significantly different for PV cells when compared by region (Supplementary Table 1, bottom). Despite expressing similar passive features in LEC and SS Ctx (e.g., membrane capacitance; 70.17 ± 5.46 pF vs. 71.91 ± 9.51 pF; LEC vs SS respectively, Supplementary Table 1), their starkly divergent excitability suggests unique molecular signatures which may also underlie differential vulnerability in AD and other diseases.

We next sought to examine differences in the molecular signature of PV interneurons in each of these regions. Single-neuron transcriptomics is a sound method for uncovering molecular diversity between different brain cell types. Nonetheless, the functional relevance of these studies is limited by substantial discordance between mRNA and protein in neurons[19]. Thus, we opted to isolate the native-state proteomes of PV interneurons from each region using our recently developed neuron-type-specific TurboID method[20] (Fig. 1i). This was achieved through systemic AAV injections to achieve whole-cortex expression of a PV-specific, Cre-expressing enhancer-AAV in Flex.TurboID mice[21] followed by region-specific microdissection (Fig. 1i; Supplementary Fig. 1a).

Flex.TurboID mice express an engineered biotin ligase (TurboID) in a cell-specific manner. After recombination, TurboID will efficiently label the extranuclear proteins in cell types of interest. Thus when coupled with subdissection, region- and cell-specific proteomic analyses can be performed. Over 800 proteins were biotinylated in PV interneurons in each region, of which nearly two hundred proteins showed region-specific differential abundances (unadjusted $p < 0.05$ $n = 207$; $n = 185$ below the permFDR 0.05 threshold; Supplementary Data 1; Fig. 1j). Generally, LEC PV interneuron proteomes showed biased enrichment in transmembrane and synaptic ion channels and transporters, while SS PV interneuron proteomes showed biased enrichment in microtubule binding, glycolysis, and fatty acid metabolism-related proteins (Supplementary Fig. 1b).

Relationships between PV interneuron proteomic signatures with cognitive resilience in human AD

We next considered whether PV interneuron proteins differentially expressed by region (Fig. 1j) were representative of proteins associated with cognitive stability during aging. To achieve this, we used data from a protein-wide association study of cognitive resilience from human brain samples (Religious Orders Study and the Rush Memory and Aging Project; 'ROSMAP'[22]). In this study, rate of cognitive decline (cognitive slope) was correlated with post-mortem brain protein levels quantified by mass spectrometry, identifying proteins positively associated with cognitive stability (pro-resilience proteins) and those negatively associated with cognitive stability (anti-resilience proteins) (Fig. 1k). We found that wild-type LEC PV interneurons displayed significantly more 'pro-resilience'-associated proteins as compared to SS Ctx PV interneurons ($p = 0.0011$; Mann-Whitney test; Fig. 1k). As nearly all the LEC PV interneuron enriched proteins were associated with cognitive stability during aging, we next explored whether expression of these enriched proteins was perturbed throughout stages of AD pathology.

We examined whether expression of these enriched proteins was perturbed throughout stages of AD pathology in humans. While several proteomics surveys of post-mortem brain tissues from AD and control brain have been performed, few studies have published data comparing the entorhinal cortex (EC) to neocortical regions, such as the frontal cortex (FC). This is true particularly regarding disease staging. In a recent study[23], EC and FC regions from post-mortem brains of control and AD cases (BRAAK stages I-III [early] and IV-VI [late]) were analyzed by quantitative MS. This yielded 737 differentially-enriched proteins (DEPs) comparing AD to control, at either early (BRAAK I-III) or late (BRAAK IV-VI) stages, which were significant in either EC or FC regions. Among these, 93 human DEPs were observed in our PV-CIBOP proteome (Supplementary Fig. 2a, Supplementary Data 2). Of these, 23 proteins showed differential levels in SS Ctx PV-INs as compared to LEC PV-INs (Supplementary Fig. 2b). Surprisingly, of the regional PV-IN proteins that were altered in human AD brain, many were pro-resilience proteins. Importantly, the LEC-enriched PV-IN proteins (including pro-resilience proteins) showed decreased levels in the EC of human AD cases (Supplementary Fig. 2b). Thus, resilience factors in PV-INs of the entorhinal cortex may be lost as AD pathology advances.

Based on observed associations between regional proteomic signatures of PV interneurons with cognitive resilience and with early changes occurring in human AD brain, we further assessed relationships between regional proteomic signatures of PV interneurons with APP and Tau protein-protein interactomes. Many APP-interacting proteins have been identified. Of 243 APP interactors identified from physical protein-protein interactors listed in the STRING database, 31 APP interactors were identified in PV-CIBOP proteomes. From these, 14 proteins were highly enriched regionally in PV interneurons. 10 proteins were highly enriched in SS Ctx PV interneurons (including Numbl, Snca, Mapt, Bin1, Hspd1, Hspa4, Hspa8, Eno1, Gapdh, Mapk3) (Supplementary Fig. 3a) and 4 were enriched in LEC PV-INs (Apoo, Grin1,

https://doi.org/10.1038/s41467-024-52297-3

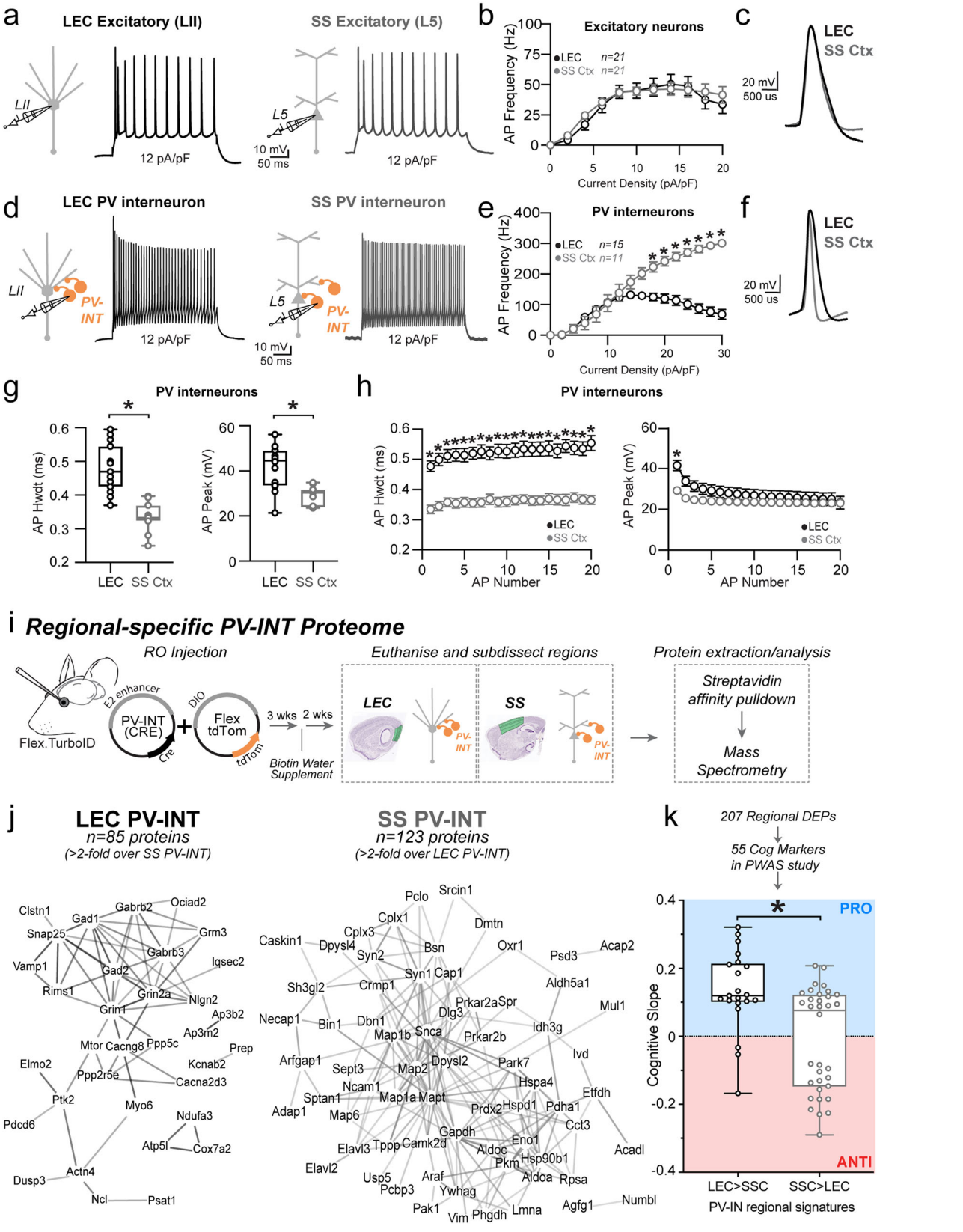

Clstn1, Grin2a) (Supplementary Fig. 3a, Supplementary Data 3). However, these physical associations may be altered in AD with either altered APP expression or mutations in the APP gene.

In a consensus analysis of tau protein interactors[24], over 2000 tau protein interactors were identified across seven human post-mortem proteomics studies. Of these, 261 proteins were identified consistently as interactors (represented in at least three of the studies), comprising a high-confidence list of tau interactors. These proteins, as previously described[24], were enriched in proteins involved in protein translation, mRNA processing and splicing, protein folding, intracellular transport, proteasome assembly, and glycolysis. In our work, 107 of these were labeled by CIBOP in PV

Fig. 1 | PV-INTs in an AD vulnerable region display reduced baseline firing. Graphical summary of AAV.E2.tdTom stereotactic injection in either the Lateral Entorhinal Cortex or Somatosensory cortex. PV-interneurons were fluorescently targeted for whole-cell current clamp recordings (**d**) as well as nearby excitatory cells (**a**). AP firing elicited by square pulse current injections of varying magnitude normalized to cellular capacitance during recording in excitatory cells (**a**) and PV-interneurons (**d**) mice from L2 LEC (left) and L5 SS Ctx (Right) at 12 pA/pF. **b** Group data summary of AP firing frequency in WT mice. Excitatory cells between LEC and SS Ctx showed no difference in AP Frequency (Hz) Ctx (LEC: Max: 50.42 ± 5.63 Hz, SS Ctx: Max: 46.35 ± 5.51 Hz, $p = 0.46$). **c** AP waveforms of excitatory cells were compared at 12 pA/pF square pulse injections in WT mice from L2 LEC and L5 SS Ctx. Aps from the 1st spike in the train are superimposed for comparison. **e** Group data summary of AP firing frequency in WT mice. PV interneurons in L2 LEC show a strong reduction in AP max firing frequency at higher current densities when compared to PV interneurons of L5 SS Ctx (LEC: Max: 131.6 ± 11.48 Hz, SS Ctx: Max: 301.1 ± 27.59 Hz, $p = <0.0001$ for 16 pA/pF and above). **f** AP waveforms of tdTom+ PV interneurons were compared at 12 pA/pF square pulse injections in WT mice from L2 LEC and L5 SS Ctx. Aps from the 1st spike in the train are superimposed for comparison. **g** Summary data of AP properties. L2 LEC PV interneurons display a significantly increased AP peak (LEC: 41.86 ± 2.66 pA, minimum: 21.33, 25% percentile: 33.47, Median: 44.53, 75% percentile: 49.12, maximum: 56.17, range: 34.84; SS Ctx: 28.75 ± 1.30 pA, minimum: 23.57, 25% percentile: 23.73, Median: 30.34, 75% percentile: 31.76, maximum: 34.89, range: 11.33; $p = 0.0002$, t = 4.83, df = 24, two-tailed unpaired *t*-test) and AP Hwdt (LEC: 0.48 ± 0.02 ms, minimum: 0.37, 25% percentile: 0.43, median: 0.47, 75% percentile: 0.55, maximum: 0.60, range: 0.23; SS: 0.33 ± 0.01 ms, minimum: 0.25, 25% percentile: 0.32, median: 0.33, 75% percentile: 0.37, maximum: 0.40, range: 0.15; $p = <0.0001$, $t = 6.10$, df = 25) for the first AP of the spike train. Individual data points (technical replicates, LEC $n = 15$, SS Ctx $n = 11$) and box plots are displayed. Significance is defined as $p < 0.05$, unpaired *t*-test. **h** Relationship between AP peak or width, in WT mice and AP # during spike trains elicited with a 12 pA/pF current injection. Data are averages of technical replicates, LEC $n = 15$, SS Ctx $n = 11$. For AP peak $p < 0.0001$, AP hwdt $p < 0.0001$. **i** Experimental approach for Regional-specific PV-interneuron Proteomes: E2 enhancer Cre AAV was retro-orbitally delivered to WT (Control) or Rosa26TurboID/wt (PV-CIBOP) mice ($n = 3$ per genotype, including males and females) followed by 3 weeks of Cre-mediated recombination, and 2 additional weeks of biotin supplementation (drinking water). The brain was then microdissected into LEC and SS Ctx and prepared for biochemical studies. **j** STRING analysis of PV-enriched proteins for LEC PV-INTs (left) and SS Ctx PV-INTs (right) (>2-fold enriched over other region) shows synaptic receptors, synaptic vesicle and exocytosis related proteins including GAD1/2, GABAb2/3, and complexins. **k** Enrichment of PWAS-identified proteins associated with cognitive slope in LEC (left) or SS Ctx (right) PV-enriched proteomic signatures. Cognitive slope was estimated in ROSMAP cases. Positive slope indicates cognitive stability or resilience when proteins are present while a negative slope indicates cognitive decline when proteins are present. Proteins positively correlated with cognitive slope are referred to as pro-resilience proteins while those negative correlated with cognitive slope are anti-resilience proteins. Enrichment of previously identified 'pro' and 'anti' resilience proteins within the PV protein dataset identified by CIBOP were assessed after weighting based on strength of association between proteins and cognitive slope. (LEC: 0.13 ± 0.03 and SS Ctx: −0.01 ± 0.03; $p = 0.001$, $t = 3.71$, df = 53, two-tailed Mann Whitney test). Proteins are derived from four biological replicates for each group. For **b**, **e**, and **h**: For all summary graphs, data are expressed as mean (± SEM). Statistical significance is denoted as $^*p < 0.05$, as determined by Two-way ANOVA with Sidak's multiple comparison test. For **g**, **k**: For all summary graphs, data are expressed as mean (± SEM). Also see Supplementary Fig. 1 for related analyses and datasets. Source data are provided as a Source Data File.

interneurons (Supplementary Data 3, 4). Of these, 32 proteins had higher levels in SS Ctx PV interneurons, 8 with higher levels in LEC PV interneurons, while 67 did not show regional differences (Supplementary Fig. 3b). In contrast, non-tau interactors were more evenly distributed across SSC and LEC PV interneurons. This result suggests that tau interactors are present at higher levels in PV-INs located in the SS Ctx as compared to those in the LEC (Chi square statistic 20.7, $p = 0.00032$). This seems to be consistent with higher levels of MAPT in SS Ctx PV interneurons as well. Tau interactors in SS Ctx PV interneurons included 14-3-3 proteins, heat shock proteins, extracellular vesicle proteins, actin/cytoskeletal proteins and RNA binding proteins. Whether the higher abundance of MAPT and tau interactors in SS Ctx PV interneurons influences the circuit's resilience to hyperexcitability at early time points is unclear. To further explore differential responses of PV interneurons between the LEC and neocortex, we utilized a model of adult-onset induction of AD-related pathology which could be regionally and temporally controlled.

Adult-onset human APP expression reduces PV interneuron excitability specifically in LEC

Traditional rodent models of AD express various (typically mutant) forms of hAPP (and related processing proteins), with transgene expression beginning while neuronal circuits are still maturing, and also in a brain-wide fashion. To eliminate the substantial network effects of hAPP during development[25] and to assess inherent vulnerability of individual areas independently, we used an adult-onset, region-specific AAV approach. To explore whether differences in basal excitability and proteomic signatures of PV interneurons described early conferred region-specific vulnerability in an AD pathology context, we virally expressed wild-type hAPP in either the LEC or SS Ctx in 8–12 week old (adult) mice. Full length hAPP (hAPP 770) (NM_000484.4), an isoform showing increased expression in human AD[26,27] was expressed using the pan-neuronal EF1a promoter (Fig. 2a; AAV.Ef1a.hAPP). We assessed the impact of this hAPP isoform on PV interneurons in the LEC and SS Ctx independently after 2-3 weeks of expression.

In LEC PV interneurons, we observed a dramatic reduction in PV interneuron firing (Fig. 2b, c) potentially related to a reduction in input resistance (Fig. 2d), as no other relevant factors (e.g., AP waveform, RMP, AP threshold, Membrane capacitance) (Fig. 2d; Supplementary Fig. 4) were affected. Using unsupervised clustering of LEC 'fast-spiking' interneuron biophysical features, control- and hAPP-expressing PV interneurons clustered separately (Supplementary Fig. 12b). By contrast, PV interneurons in the SS Ctx displayed no change in firing rate (Fig. 2g) despite an increase in the AP AHP (Supplementary Fig. 5d). All other active and passive features were unchanged in SS Ctx (Fig. 2h; Supplementary Fig. 5b–e). The presence of hAPP mRNA and protein was confirmed in PV neurons 2-3 weeks after viral injection (Fig. 2i, j; Supplementary Fig. 6) using RNAscope and PV-specific flow cytometry respectively. Together, the intrinsic excitability of PV interneurons was significantly reduced in the LEC, but not SS Ctx, following hAPP expression.

Adult-onset murine APP expression does not affect PV interneuron physiology

Several studies of different mouse models of APP-related pathology report altered intrinsic excitability in GABAergic intereneurons[7–10,13]. Whether this is simply a result of hAPP overexpression[28] during development or effects of its downstream cleavage products remain controversial. To address this, we next injected a virus containing full-length murine APP (mAPP) (NM_001198823.1) (Fig. 3a; AAV.Ef1a.mAPP) into the LEC. Despite a significant increase of mAPP expression over endogenous background levels (Supplementary Fig. 8d, e), changes in PV interneuron firing and input resistance seen following hAPP expression (Fig. 2) were absent following 2-3 weeks of viral mAPP expression (Fig. 3b, c; Supplementary Fig. 8b, c). Importantly, RNAscope studies confirmed that the magnitude of AAV-induced mAPP expression was similar to that of hAPP in earlier experiments (Fig. 3d), indicating that the differential physiological effects were not due to variability in APP expression levels. Furthermore, as we saw no alterations in the somatosensory cortex PV-interneurons after hAPP expression, we conclude this differing response is not due to a specific

https://doi.org/10.1038/s41467-024-52297-3

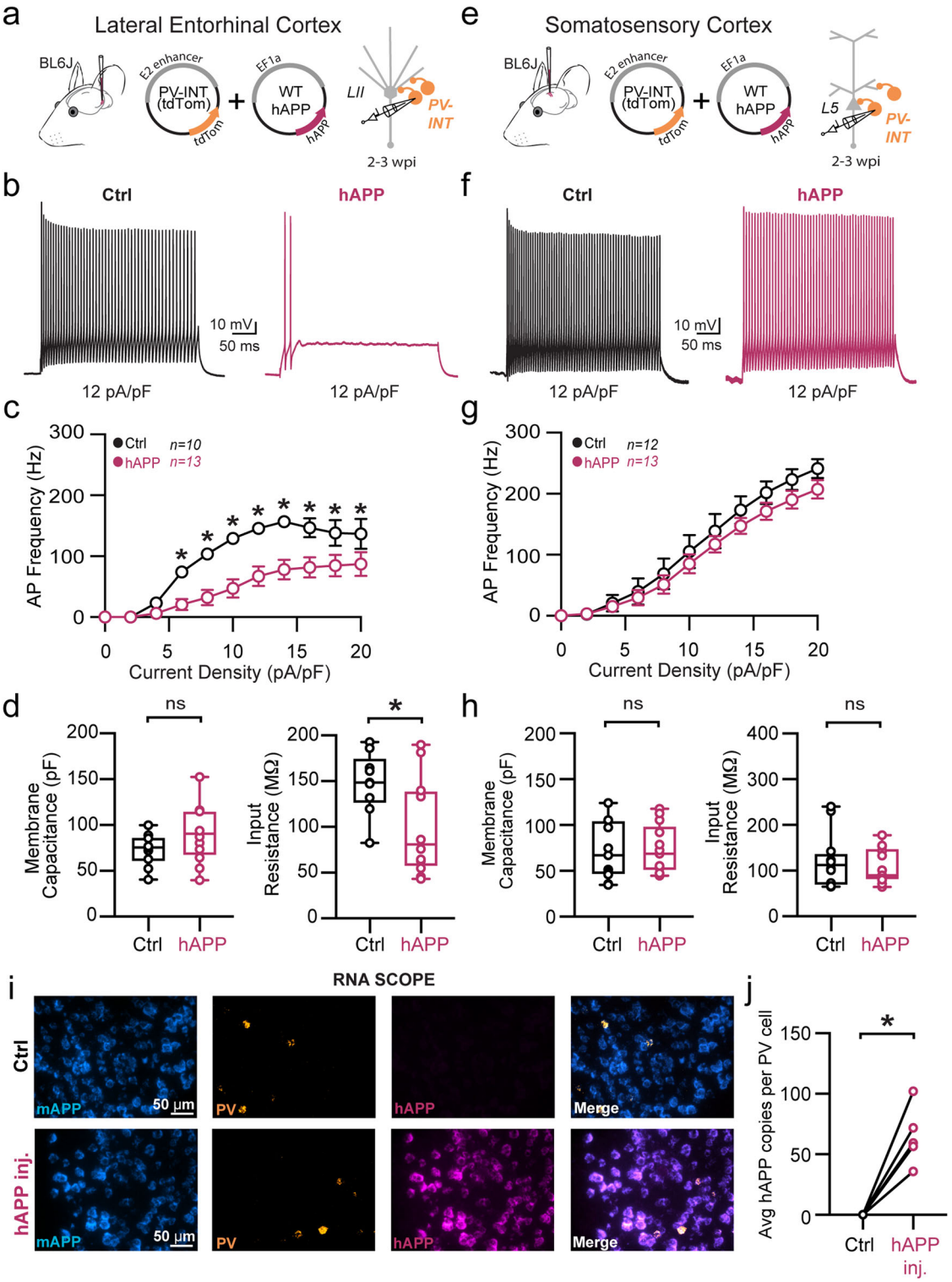

inflammatory effect of the human protein alone. Thus, hAPP-induced dysfunction of LEC PV interneurons cannot be explained by overexpression of APP alone.

Murine APP with a humanized amyloid-beta sequence moderately impairs PV interneurons

We next investigated whether the effect of hAPP on PV interneuron function could be explained by the differences in the amyloid-beta sequence of the human and mouse genes. To address this, we cloned the full-length murine APP (mAPP) (NM_001198823.1) but humanized the three differing amino acids in the amyloid-beta sequence, G676R, F681Y, and R684H (Fig. 3e; AAV.Ef1a.mAPP/hAβ Chimera). After AAV-directed expression of this APP Chimera in the LEC for 2-3 weeks, we observed a reduction in PV interneuron firing (Fig. 3f, g). However, the mAPP/hAβ effect was less robust when compared to the fully human version (Fig. 3h; Supplementary Fig. 9d) and appeared to manifest in a mechanistically distinct fashion relative to hAPP (Supplementary Fig. 9). Thus, the contribution of the human amyloid-beta sequence leads to PV-interneuron hypofunction, but was not sufficient to induce the more drastic reduction seen with full-length human hAPP. Finally, to further evaluate a role Aβ in this process, we tested the effect of exogenous Aβ ($Aβ_{1-40,1-42}$; 0.25 µM; 3 h)

Fig. 2 | Adult-onset human APP expression reduces LEC PV interneuron excitability. a Graphical summary of AAV.E2.tdTom and AAV.EF1a.hAPP (or for Ctrl, saline) stereotactic injection in the Lateral Entorhinal Cortex. PV-interneurons were fluorescently targeted (tdTom +) for whole-cell current clamp recordings. **b** AP firing elicited by square pulse current injections of varying magnitude normalized to cellular capacitance during recording in tdTom+ PV-INT from L2 LEC at 12 pA/pF. **c** Group data summary of AP firing frequency in L2 LEC from Ctrl (black) and hAPP injected mice (magenta). LEC PV interneurons from hAPP injected mice show a significant reduction in AP Frequency (Hz) when compared to Ctrl(Ctrl: Max: 156.6 ± 13.52 Hz, hAPP: Max: 91.84 ± 8.74 Hz, $p < 0.0001$, Two-Way ANOVA). **d** Summary data of AP properties. L2 LEC PV interneurons after hAPP injection display a significantly decreased input resistance (Ctrl: 145.7 ± 11.61 MΩ, minimum: 82.33, 25% percentile: 125.8, median: 148.4, 75% percentile: 175.3, maximum: 192.9, range: 110.6; hAPP: 88.78 ± 15.11 MΩ, minimum: 43.02, 25% percentile: 56.95, median: 80.93, 75% percentile: 139.1, maximum: 189.9, range: 146.8; $p = 0.01$, $t = 2.73$, df = 21) and an insignificant increase in membrane capacitance (Ctrl: 68.83 ± 5.34 pF, minimum: 40.49, 25% percentile: 60.14, median: 75.62, 75% percentile: 86.40, maximum: 99.78, range 59.26, hAPP: 90.21 ± 9.77 pF, minimum: 39.90, 25% percentile: 66.88, median: 90.51, 75% percentile: 115.2, maximum: 152.4, range: 112.5; $p = 0.07$, $t = 1.92$, df = 21). **e**. Graphical summary of AAV.E2.tdTom and AAV.EF1a.hAPP (or for Ctrl, saline) stereotactic injection in the Somatosensory Cortex. PV-interneurons were fluorescently targeted (tdTom +) for whole-cell current clamp recordings. **f** AP firing elicited by square pulse current injections of varying magnitude normalized to cellular capacitance during recording in tdTom+ PV-INT from L5 SS Ctx at 12 pA/pF. **g** Group data summary of AP firing frequency in L5 SS Ctx from Ctrl (black) and hAPP injected mice (magenta). SS Ctx PV interneurons from hAPP injected mice show no significant change in AP Frequency (Hz) when compared to Ctrl (Ctrl: Max: 301.1 ± 27.59 Hz, hAPP: Max: 257.2 ± 24.06 Hz). **h** Summary data of AP properties. SS Ctx interneurons after hAPP injection display an unchanged Membrane Capacitance (Ctrl: 71.91 ± 9.514, minimum: 34.82, 25% percentile: 46.09, median: 67.31, 75% percentile: 104.9, maximum: 124.2, range 89.40; hAPP: 73.14 ± 7.327, minimum: 44.84, 25% percentile: 50.37, median: 68.69, 75% percentile: 98.70, maximum: 117.7, range: 72.83; $p = 0.9180$, t = 0.1041, df = 23) and input resistance (Ctrl: 121.2 ± 17.14, minimum: 65.09, 25% percentile: 68.17, median: 112.1, 75% percentile: 137.5, maximum: 240.6, range: 175.5; hAPP: 109.1 ± 10.56, minimum: 64.34, 25% percentile: 80.07, median: 89.76, 75% percentile: 148.6, maximum: 177.9, range: 113.6; $p = 0.5475$, t = 0.6106, df = 23). **i** RNAscope representative images at 40x magnification for Ctrl injected (top) and hAPP injected mice (bottom): mAPP mRNA (cyan), Parvalbumin mRNA (gold), human APP mRNA (magenta), and a final merged image. **j** RNAscope quantification for hAPP copies per PV+ cell comparing control to hAPP injected. hAPP injected show a significant increase in hAPP copies per PV+ cell ($p = 0.0039$, $t = 5.987$, df = 4; two-tailed paired t-test). For all summary graphs, data are expressed as mean (± SEM). For **c**, **g**, and **i**: Statistical significance is denoted as $^*p < 0.05$, as determined by Two-way ANOVA with Sidak's multiple comparison test. For d, h: Individual data points (technical replicates, LEC: Ctrl $n = 10$, hAPP $n = 13$; SS: Ctrl $n = 12$, hAPP $n = 13$; all data collected from 3 biological replicates each) and box plots are displayed. Statistical significance is denoted as $^*p < 0.05$, as determined by two-tailed unpaired *t*-test. Source data are provided as a Source Data File.

incubation on PV interneurons in the LEC. Similar to hAPP, Aβ incubation alone also induced a robust reduction in AP firing (Supplementary Fig. 9f).

Adult-onset human APP expression does not affect excitatory cell intrinsic properties

Because recent studies using different mouse models of APP/Aβ pathology report altered intrinsic excitability of excitatory neurons[25,29], we also assessed the effects of 2-3 weeks of hAPP expression on principal excitatory cells in the LEC and SS Ctx (Fig. 4a–e). Consistent with unaltered PV firing in SS Ctx, no change in intrinsic firing frequency or passive properties were noted in pyramidal cells in the SS Ctx (Fig. 4f–h; Supplementary Fig. 11). Surprisingly, we also observed no impact of hAPP on intrinsic AP firing of LII LEC excitatory neurons (Fig. 4b, c). Further, membrane capacitance was unperturbed (Fig. 4d) suggesting no major alterations to LII cellular morphology. A modest but significant increase in dV/dt max was noted in LEC LII principal cells (Supplementary Fig. 10d), potentially via an hAPP-dependent modulation of Na_v channels in these cells. All other active and passive properties were unaltered (Fig. 4d; Supplementary Fig. 8). Importantly, RNAscope experiments confirmed increased hAPP expression in CaMKIIa+ cells (Fig. 4i, j), indicating that our AAV also targeted excitatory neurons as expected. Using principal component analysis (PCA) of several excitatory cell biophysical features from LEC recordings, clusters could be separated based on input resistance, membrane time constant, and resting membrane potential. These clusters likely arise due to sampling of both LII fan cells and LII pyramidal cells[30], suggesting our population of principal cells likely included both cell types (Supplementary Fig. 12a). When assessed, these excitatory populations showed no differential clustering when expressing hAPP (Supplementary Fig. 12a). Together, these results indicate that principal neurons are more resistant to changes in their intrinsic excitability following adult-onset hAPP expression compared to PV interneurons.

hAPP expression induces basal circuit hyperexcitability in the LEC but not SS Cortex

Although we observed no alterations in the intrinsic excitability of excitatory cells in either region following hAPP expression, we wanted to assess whether the changes in PV interneuron biophysics in LEC had an impact on local circuit activity. To examine this at population level, we acquired spontaneous post-synaptic currents from principal cells in either region (Fig. 5a–d). In the LEC, spontaneous inhibitory event (sIPSC) frequency was significantly decreased (increase in the mean inter-event interval [IEI]) after 2-3 weeks of hAPP expression (Fig. 5b, c). Furthermore, we analyzed the LEC sIPSCs for differences in the frequency in small and large amplitude events (cutoff 40 pA derived from a previously published method[31]), to determine if the increase in sIPSC IEI was related to distal inhibition (small amplitude) or proximal, perisomatic inhibition (large amplitude). We observed that while the frequency of small amplitude events was unchanged ($p = 0.52$, two-tailed unpaired *t*-test, $t = 0.65$, df = 18; Ctrl: 1.66 ± 0.36 Hz, hAPP: 1.33 ± 0.35 Hz), the frequency of large amplitude events was significantly decreased in the LEC ($p = 0.02$, two-tailed unpaired *t*-test, $t = 2.51$, df = 18; Ctrl: 4.66 ± 1.1 Hz; hAPP: 1.74 ± 0.49 Hz), indicating a selective effect on peri-somatically innervating inhibitory neurons. In layer II of the entorhinal cortex, Reelin+ excitatory cells receive perisomatic inhibition primarily from PV interneurons, rather than CCK basket cells[17,32]. Thus these results are consistent with a reduction in intrinsic PV excitability. In an apparent response to this reduced inhibitory tone, spontaneous excitatory event (sEPSC) frequency increased in the LEC following hAPP expression (Fig. 5b, c). In contrast to the LEC, recordings from SS Ctx (Fig. 5d, e) revealed no change in sIPSC or sEPSC frequency following hAPP expression (Fig. 5f), in agreement with the lack of changes in intrinsic excitability in the SS Ctx shown earlier. Spontaneous and miniature (excitatory or inhibitory) synaptic amplitudes in the LEC and SS Ctx were unchanged in either region (Supplementary Fig. 13), indicating that postsynaptic receptor alterations did not arise in excitatory neurons following short-term adult-onset hAPP expression. mIPSC and mEPSC frequencies were also unaltered, suggesting no change in the number of inhibitory or excitatory synapses at this point (Supplementary Fig. 13b). Together, these results indicate that basal circuit activity in the LEC, but not SS Ctx, becomes hyperexcitable following short-term hAPP expression, likely resulting from a region-specific PV interneuron vulnerability.

hAPP-induced network dysfunction is attenuated following PV interneuron activation in vivo

To understand how short-term expression of hAPP affected network behavior in vivo, we next performed local field potential (LFP)

https://doi.org/10.1038/s41467-024-52297-3

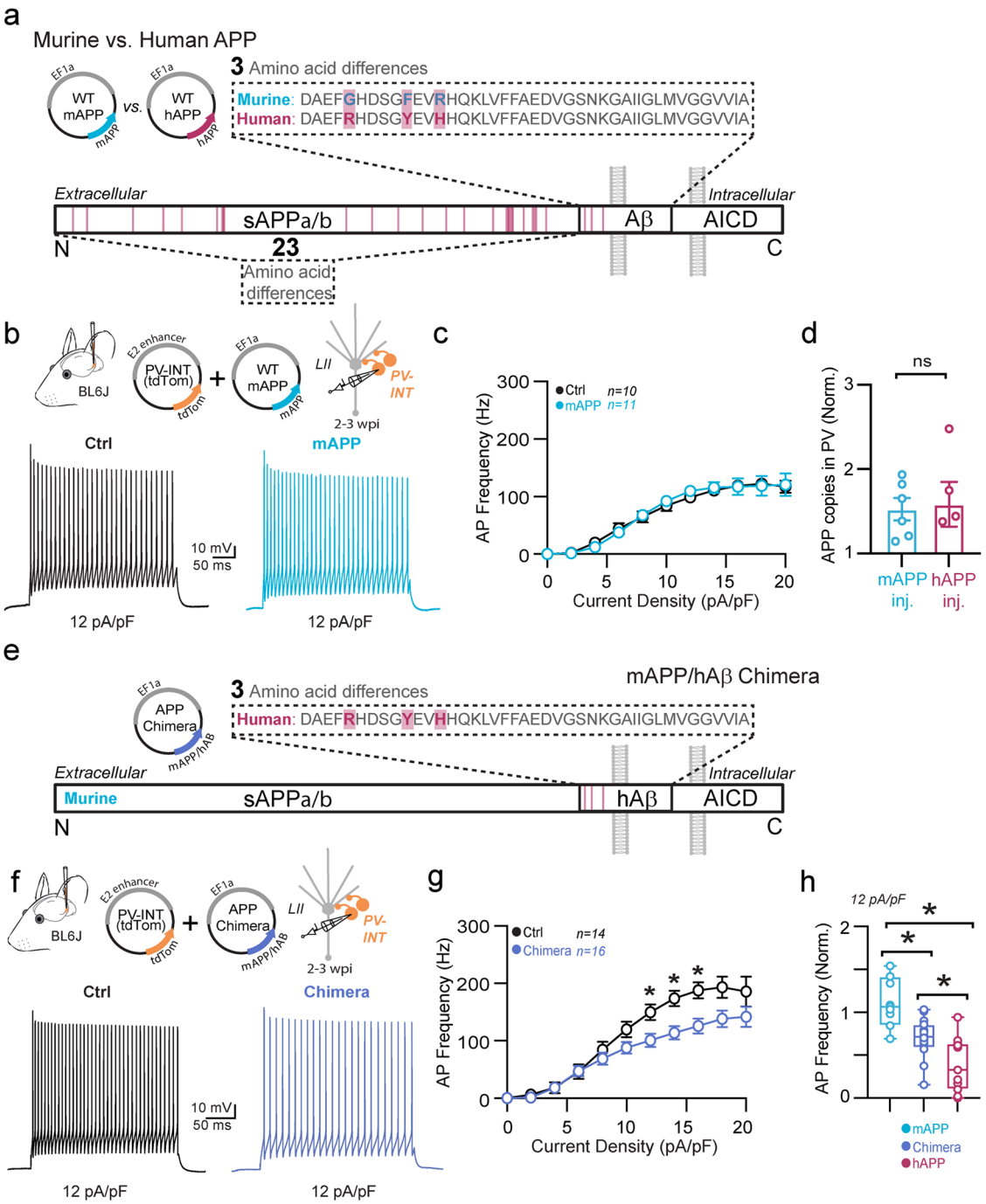

recordings in the LEC of lightly anesthetized, head-fixed mice 3 weeks after injection of hAPP or control (tdTom) virus (Fig. 6a–c). As predicted by our ex vivo studies, we found a broad increase in activity across several frequency domains, similar to previous findings in the LEC of a sporadic AD model[15]. Notably, the delta, theta, and low gamma frequency domains showed significant increases in power (Fig. 6e) indicating increases in neuronal activity[33] (Supplementary Fig. 14b). Despite following a similar trend, frequency domains above 80 Hz (i.e., high Gamma and beyond) were not significantly altered (Fig. 6e, Supplementary Fig. 14b). Together with our mechanistic evaluations earlier, this suggests that hAPP-induced PV interneuron dysfunction induces network hyperexcitability in vivo.

We next asked whether 'real-time' enhancement of PV interneuron excitability could ameliorate hAPP-induced network hyperexcitability in vivo. To accomplish this, PV interneurons in the LEC were activated chemogenetically using the E2 PV-specific targeting enhancer[18] to express hM3Dq.DREADD (Gq.DREADD). For DREADD experiments, groups are denoted as either Ctrl (Gq.DREADD/no hAPP) or hAPP (Gq.DREADD + hAPP) (Fig. 6f, h, j). Remarkably, chemogenetic activation of PV interneurons with low-dose CNO (0.5 mg/kg) could rapidly restore the hyperexcitable LFP in hAPP-expressing mice to Ctrl levels (Fig. 6g, h) most notably in the delta (Fig. 6i) and theta (Fig. 6k). Perhaps surprisingly, 0.5 mg/kg CNO did not significantly reduce LFP power in Ctrl (no hAPP) animals with respect to saline. Importantly, DREADD expression itself or CNO administration without DREADD expression did not alter LFP power in either the Ctrl or hAPP animal groups (Supplementary Fig. 14c, d). Thus chemogenetic enhancement of PV interneurons in the LEC was sufficient to completely rescue the hAPP-induced hyperexcitability in vivo.

Fig. 3 | Murine APP does not affect PV interneuron physiology, but mAPP/hAB chimera replicates partial findings of hAPP-induced deficits. a Pictorial representation of differing amino acids between murine APP and human APP proteins; 26 different amino acids in total, 3 of which are in the amyloid-beta segment of the protein. **b** Graphical summary of AAV.E2.tdTom and AAV.EF1a.mAPP (or for Ctrl, saline) stereotactic injection in the Lateral Entorhinal Cortex. PV interneurons were fluorescently targeted for whole-cell current clamp recordings. AP firing elicited by square pulse current injections of varying magnitude normalized to cellular capacitance during recording in PV interneurons from Ctrl (left) and mAPP injected (right) L2 LEC at 12 pA/pF. **c** Group data summary of AP firing frequency in Ctrl and mAPP injected mice. PV interneurons between Ctrl and mAPP injected showed no difference in AP Frequency (Hz) (Ctrl: Max: 122.3 ± 11.11 Hz, mAPP: Max: 120.6 ± 11.50 Hz, $p = 0.95$). Statistical significance is denoted as $^*p < 0.05$, as determined by Two-way ANOVA with Sidak's multiple comparison test. **d** RNAscope quantification for APP copies per PV+ cell with APP injected (mAPP or hAPP) each normalized to their contralateral hemisphere average endogenous murine APP copy per PV+ cell. mAPP injected and hAPP injected mice show similar increases in increased APP expression. copies per PV+ cell ($p = 0.84$, $t = 0.21$, df = 9; two-tailed unpaired t-test), data points represent biological replicates; mAPP $n = 6$, hAPP $n = 5$. **e** Pictorial representation of the resultant Chimera protein; murine APP with a humanized amyloid-beta segment. **f** Graphical summary of AAV.E2.tdTom and AAV.EF1a.mAPP/hAB Chimera (or for Ctrl, saline) stereotactic injection in the Lateral Entorhinal Cortex. PV interneurons were fluorescently targeted for whole-cell current clamp recordings. AP firing elicited by square pulse current injections of varying magnitude normalized to cellular capacitance during recording in PV interneurons from Ctrl (left) and Chimera injected (right) L2 LEC at 12 pA/pF. **g** Group data summary of AP firing frequency in Ctrl and Chimera injected mice. PV interneurons between Ctrl and mAPP injected showed no difference in AP Frequency (Hz) (Ctrl: Max: 193.6 ± 19.47 Hz, mAPP: Max: 145.4 ± 14.05 Hz, $p < 0.0001$; for 12 pA $p = 0.0378$, for 14 pA $p = 0.0368$, for 16 pA $p = 0.0426$). Statistical significance is denoted as $^*p < 0.05$, as determined by Two-way ANOVA with Sidak's multiple comparison test. **h** Comparison of PV interneuron firing frequencies expressing mAPP, mAPP/hAB Chimera, or hAPP normalized to their dataset controls at 12 pA/pF. Statistical significance is denoted as $^*p < 0.05$, as determined by Ordinary one-way ANOVA with Tukey's multiple comparisons test. (mAPP vs. Chimera: $p = 0.0011$, mAPP vs. hAPP: <0.0001, Chimera vs. hAPP: $p = 0.0335$; df = 35), data points represent technical replicates (cells) normalized to their own group controls, mAPP $n = 11$, Chimera $n = 16$, hAPP $n = 11$. Box plots (mAPP: minimum: 0.6925, 25% percentile: 0.8446, median: 1.065, 75% percentile: 1.420, maximum: 1.541, range: 0.8487; Chimera: minimum: 0.1538, 25% percentile: 0.5879, median: 0.7143, 75% percentile: 0.8571, maximum: 1.033, range: 0.8791; hAPP: minimum: 0.0000, 25% percentile: 0.1022, median: 0.3292, 75% percentile: 0.6360, maximum: 0.9407, range: 0.9407). For all summary graphs, data are expressed as mean (± SEM). Source data are provided as a Source Data File.

hTau co-expression with hAPP quells LEC hyperexcitability at the cost of increased pathological tau species

Beyond hyperexcitability, the LEC is also the first cortical region to develop tau pathology[1,34–37]. Although Alzheimer's is characterized by early hAPP/Aβ and later Tau pathology, respectively, the relationship between hAPP, hyperexcitability, and Tau remains unclear. It has previously been established that artificially increasing neuronal activity can accelerate tau pathology[38–40]. However, long-term transgene expression of human Tau (hTau) may act to dampen circuit excitability[16,41,42] (but see ref. 43). Thus, we sought to assess the interplay of hAPP-induced circuit hyperexcitability and hTau expression in the LEC. To achieve this, we packaged full-length wild-type human Tau (hTau) into a separate AAV to induce Tau expression locally in the entorhinal cortex. Spontaneous post-synaptic currents were then recorded from LII principal cells, 3 weeks after hAPP alone, hTau alone, or hAPP + hTau co-injection (Fig. 7a). With hAPP, we again observed an elevated E:I frequency ratio (sEPSC frequency/sIPSC frequency, normalized to the Control dataset) as described earlier (Fig. 7b). We hypothesized that hTau would result in a reduced E:I ratio with respect to the control baseline. Although the E:I ratio with hTau alone was less than hAPP alone, E:I balance surprisingly remained unchanged with respect to the Control (Fig. 7b). However, hAPP + hTau resulted in an intermediate effect, which abolished the hyperexcitable phenotype seen with hAPP alone (Fig. 7b). These results agree with a homeostatic role for Tau in maintaining circuit excitability. Beyond synaptic event frequencies, all other spontaneous event properties (i.e., amplitude) were statistically similar between all groups (Supplementary Fig. 15a, b).

We next assessed whether the moderating effect of hTau on circuit activity came at the cost of increased pathology, using antibodies for pSer202/pThr205 phosphorylated tau (AH36) or oligomeric tau (T22). Both Control and hAPP-injected conditions showed low levels of AH36 positivity, likely due to endogenous labeling of murine tau (Supplementary Fig. 15c, d). While both hTau and hAPP+hTau induced high levels of AH36-positive staining (Fig. 7c, d), it appeared that hTau alone injected mice had mostly somatically located staining. In contrast, hAPP+hTau co-injected mice displayed disperse staining (Fig. 7c) suggesting an interaction with hAPP which promotes extracellular transport of pathological Tau. Oligomeric tau (T22) (Fig. 7e), which has recently been shown in human tissue as a tau species that may spread transsynaptically from axons to other regions[44], displayed a surprisingly robust increase, but only when hAPP+hTau were co-expressed (Fig. 7e, f; Supplementary Fig. 15e, f). Thus, it appears that co-expression of Tau could help restore APP-induced circuit hyperexcitability. However, a consequence of their co-expression appears to be the amplification and translocation of known pathological tau species.

Discussion

Here we demonstrate that PV interneurons within the LEC are biophysically distinct from other neocortical PV interneurons. Furthermore, differences in the native-state proteomes of PV interneurons from the LEC and SS Ctx regions were marked. Although the WT PV firing frequency in our LEC recordings is consistent with previous obervations[17], the striking biophysical differences (i.e., AP waveform) with respect to PV cells in other cortical regions had not been systematically evaluated. Interestingly, these LEC PV interneurons do resemble a previously observed PV+ interneuron in other regions, such as the 'quasi fast-spiking interneurons' of the subiculum[45], the 'fast-spiking-like cells' of the striatum[46], and the 'non-fast-spiking interneurons' of the CA1[47]. However, where these cells represent a small subset of the PV+ interneurons of these regions (~20% in CA1)[47], the majority of our recorded PV+ interneurons displayed this low-firing phenotype. Whether the baseline low-firing frequency of PV+ interneurons in the LEC confers vulnerability to hAPP-induced pathophysiology remains unclear. In addition to their different intrinsic features, PV interneurons of the LEC displayed a multitude of differentially expressed proteins in comparison to SS Ctx PV interneurons. Interestingly, compared to SS, we found that PV interneurons residing in the LEC were significantly enriched in proteins associated with cognitive resilience in humans. However, many of these LEC PV-IN pro-resilience proteins were altered in the entorhinal cortex of AD patients. This suggests a regional and cell-type-specific susceptibility to the progression of AD pathophysiology. Although a comparison of PV-CIBOP regional proteomes with bulk human brain proteomes gives further insight into potential cell-type-specific alterations in phases of AD, it is still limited by the inability to verify PV interneuron-specificity of observed changes in human brain. As we only recently established the first, to our knowledge, PV interneuron-specific proteome[21], we look forward to the advancement of techniques to come in order to complete such a level of analysis in human tissue. Future studies at the single-cell level in humans with early-stage AD will be necessary to confirm this assertion.

Recent work shows that APP expression moves outside of normal homeostatic levels in models of late-onset AD risk alleles[48,49]. The ratio

https://doi.org/10.1038/s41467-024-52297-3

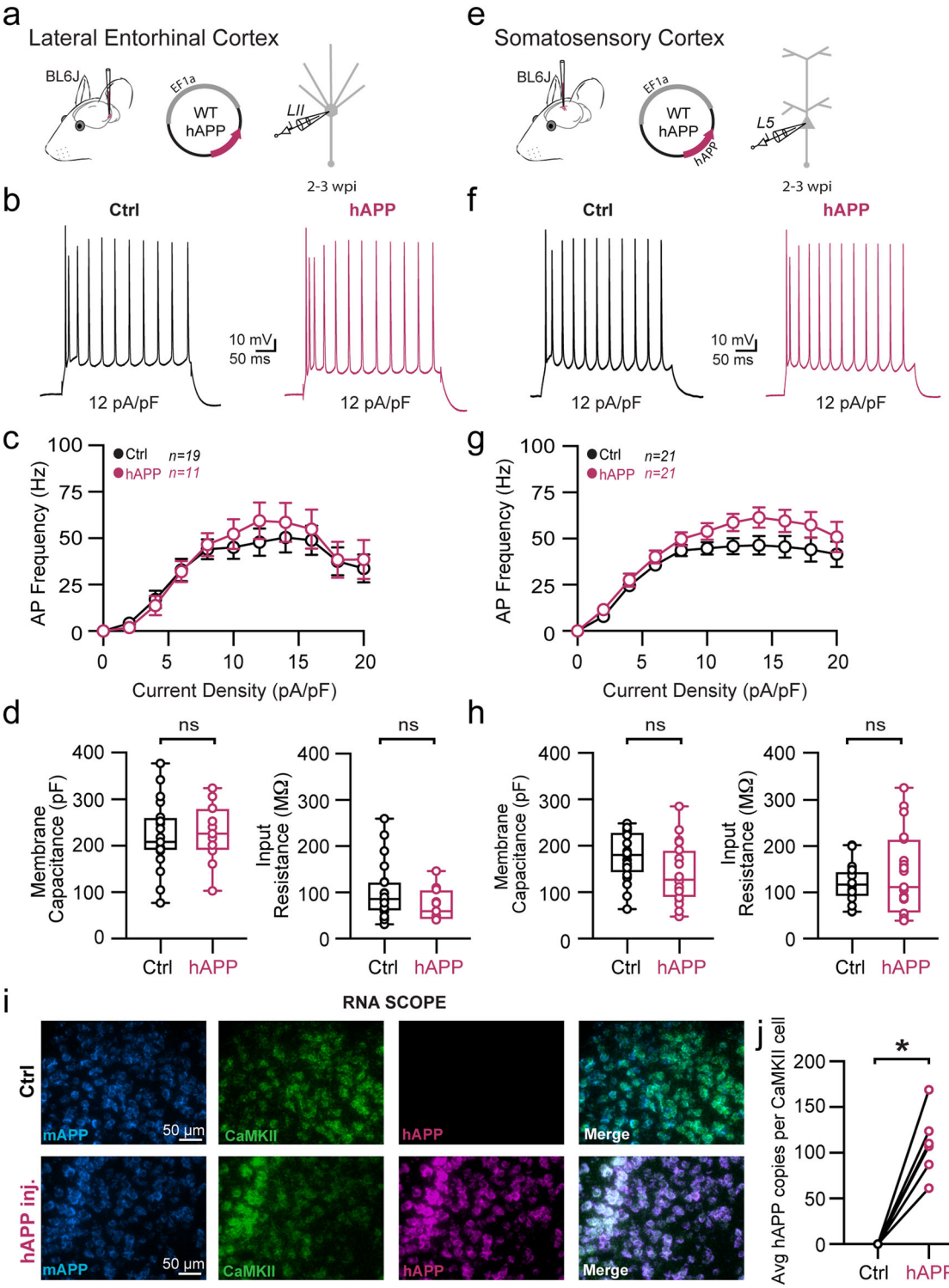

of different APP isoforms also shifts in human AD, from mainly APP 695 to increasing levels of APP 770 and 751[26,27]. These longer isoforms show increased expression following aging-related processes (e.g., after reproductive hormonal production decline[50], hypercholesterolemia[51], and atherosclerosis[52]), all of which are also associated with increased AD risk[53–56]. Thus, here we induced adult-onset expression of hAPP 770 to model these phenomena. Adult-onset expression of hAPP allowed us to avoid any alterations to neurodevelopment which may arise with expression of a transgene early in development, as many mouse models of AD exhibit. However, we acknowledge that this model does not encapsulate all alterations that may arise throughout aging and early Alzheimer's Disease. Thus, further studies must be conducted to assess these mechanisms in aging mice. At this time point, we found that shortly after hAPP expression (2-3 weeks), LEC PV interneuron firing became severely disrupted. Although viral hAPP expression was robust in both excitatory and inhibitory cells due to the generic promoter used to express hAPP in our experiments, we observed no alteration to the intrinsic excitability of excitatory cells in LEC LII. Despite this, there was a significant disruption in the E:I balance in LEC slices. Thus, we propose basal network hyperexcitability observed arises as a result of decreased PV-interneuron firing, resulting in a loss of tonic inhibition and thus, increased firing propensity of surrounding

Fig. 4 | Adult-onset human APP expression does not alter excitatory neuron physiology. a Graphical summary of AAV.EF1a.hAPP (or for Ctrl, saline) stereotactic injection in the Lateral Entorhinal Cortex. Excitatory cells were targeted for whole-cell current clamp recordings. **b** AP firing elicited by square pulse current injections of varying magnitude normalized to cellular capacitance during recording in Ctrl and hAPP injected L2 LEC excitatory cells from at 12 pA/pF. **c** Group data summary of AP firing frequency in L2 LEC from Ctrl (black) and hAPP injected mice (magenta). Excitatory neurons in L2 LEC from hAPP injected mice show no alteration in AP Frequency (Hz) when compared to Ctrl (Ctrl: Max: 50.42 ± 5.63 Hz, hAPP: Max: 59.43 ± 6.56 Hz, $p = 0.99$, df = 28). **d** Summary data of AP properties. L2 LEC excitatory cells after hAPP injection display an unchanged Membrane Capacitance ($p = 0.83$, t = 0.27, Ctrl: minimum: 77.13, 25% percentile: 189.5, median: 208.5, 75% percentile: 261.9, maximum: 377.5, range: 300.3; hAPP: minimum: 103.0, 25% percentile: 189.9, median: 226.4, 75% percentile: 281.1, maximum: 324.4, range: 221.3) as well as an unchanged input resistance ($p = 0.15$, $t = 1.50$, df = 28; Ctrl: minimum: 30.98, 25% percentile: 60.00, median: 85.43, 75% percentile: 122.9, maximum: 259.8, range: 228.9; hAPP: minimum: 40.70, 25% percentile: 41.29, median: 59.46, 75% percentile: 106.4, maximum: 146.2, range: 105.5), data points represent biological replicates; Ctrl $n = 19$, hAPP $n = 11$. **e** Graphical summary of AAV.EF1a.hAPP (or for Ctrl, saline) stereotactic injection in the Somatosensory Cortex. Excitatory neurons in L5 were targeted for whole-cell current clamp recordings. **f** AP firing elicited by square pulse current injections of varying magnitude normalized to cellular capacitance during recording in excitatory cells from L5 SS Ctx at 12 pA/pF. **g** Group data summary of AP firing frequency in L5 SS Ctx from Ctrl (black) and hAPP injected mice (magenta). SS Ctx excitatory neurons from hAPP injected mice show no significant change in AP Frequency (Hz) when compared to Ctrl (Ctrl: Max: 46.35 ± 5.38 Hz, hAPP: Max: 61.43 ± 6.78 Hz, $p > 0.05$, df = 40). **h** Summary data of AP properties. SS Ctx interneurons after hAPP injection display an unchanged Membrane Capacitance (Ctrl: 176.9 ± 11.58, hAPP: 140.5 ± 14.31, p = 0.06, t = 1.98, df = 40, two-tailed unpaired *t*-test; Ctrl: minimum: 63.66, 25% percentile: 141.4, median: 180.5, 75% percentile: 229.4, maximum: 248.3, range: 184.7; hAPP: minimum: 47.71, 25% percentile: 88.57, median: 127.2, 75% percentile: 191.3, maximum: 285.2, range: 237.5) and input resistance (Ctrl: 117.8 ± 8.93, hAPP: 140.5 ± 20.43, $p = 0.23$, t = 1.05, df=40, two-tailed unpaired *t*-test; Ctrl: minimum: 58.62, 25% percentile: 91.03, median: 117.1, 75% percentile: 145.8, maximum: 202.1, range: 143.5; hAPP: minimum: 39.12, 25% percentile: 54.81, median: 111.9, 75% percentile: 215.4, maximum: 326.2, range: 287.5) data points represent biological replicates; Ctrl n = 21, hAPP n = 21. **i** RNAscope representative images at 40x magnification for Ctrl injected (top) and hAPP injected mice (bottom(: mAPP mRNA (cyan), CaMKIIa mRNA (green), human APP mRNA (magenta), and a final merged image. **j** RNAscope quantification for hAPP copies per CaMKIIa+ cell comparing control to hAPP injected. hAPP injected show a significant increase in hAPP copies per CaMKIIa+ cell ($p = 0.0007$, $t = 7.42$, df = 5; two-tailed paired *t*-test). For all summary graphs, data are expressed as mean (± SEM). For **c**, **g** Statistical significance is denoted as $^*p < 0.05$, as determined by Two-way ANOVA with Sidak's multiple comparison test. For **d**, **h** Individual data points and box plots are displayed. Statistical significance is denoted as $^*p < 0.05$, as determined by two-tailed unpaired *t*-test. Source data are provided as a Source Data File.

excitatory neurons. Notably, our hAPP condition displayed a large peak in LFP power in the delta frequency domain (1–4 Hz) in vivo, which was returned to baseline upon rescue of PV interneuron excitability. This delta peak may represent increased low-frequency excitatory neuron synchronicity. We also observed a broadband increase in most other frequency ranges in the hAPP condition, including gamma power, which has been previously described in AD patients[57] and in amyloid pathology mouse models[13].

Of the 26 amino acids differentiating the hAPP and mAPP proteins, only 3 are situated within the amyloid-beta region. Of note, of the 'wild-type' versions of newly designed hAPP knock-in mouse models[58,59] now in wide use, only the 3 amino acids within the amyloid region are humanized. It has been shown that expression of WT hAPP can result in a substantial increase in amyloid-beta[60], suggesting that PV interneuron hypofunction in the LEC phenotype results directly from Aβ accumulation. Thus, we investigated if humanizing only the 3 amino acids could recapitulate our findings of hAPP-induced impaired PV interneuron physiology. Interestingly, the mAPP/hAβ Chimera did result in impaired PV-interneuron firing, but did not replicate the more drastic alterations seen with full-length hAPP expression. This suggests amyloid-beta is not the sole cause for early phase interneuron dysfunction, and may suggest a role for either full-length APP or its other cleavage products in this stage of the neurodegenerative cascade. Alternatively, the full-length hAPP may result in enhanced Aβ production with respect to the mAPP/Aβ chimera.

GABAergic interneurons require homeostatic APP levels for proper physiological function and circuit activity control[61]. Furthermore, APP[62], as well its cleavage proteins[63–65] and products[66,67], can modulate neuronal biophysics and alter the expression of ion channels, many of which are essential for maintaining the 'fast-spiking' phenotype of PV interneurons. Modifications to Na_v1 or K_v3 channel availability in different constitutive hAPP-expressing mice have recently been linked to reduced PV excitability[7,13]. Although short-term full-length hAPP expression in this study could significantly reduce PV firing, we observed no outward biophysical indicators implicating changes to either Na_v1 or K_v3 availability which could underlie altered PV firing in the LEC. However, this likely requires further evaluation of specific ion channel subtypes.

Although firing of PV interneurons in SS cortex were unaffected with short-term hAPP expression, we did note a change in AP threshold, potentially attributable to alterations in Na_v channels. It is likely that if expressed longer, hAPP expression in the SS Ctx may result in impaired PV interneuron excitability[7,13]. Thus, alternative biophysical mechanisms are likely responsible for our observations following short-term hAPP expression in adult mice. Notably, we observed a substantial decrease in input resistance in LEC PV cells expressing hAPP. This could be due to enhanced availability of leak channels or potentially low-voltage activating K^+ conductances, such as KCNQ (K_v7), which have been shown to be regulated by APP cleaving proteins[63] and cleavage products[66,68,69]. Interestingly, the Gq-coupled hM3Dq DREADD system increases cell excitability specifically by increasing input resistance in cells. Of note, here we show that recovery of reduced input resistance in PV interneurons through specific activation of Gq.DREADDs was sufficient to attenuate hAPP-induced hyperexcitability in the LEC in vivo.

The LEC is also the first cortical region to develop tau pathology[1,34–37]. Yet, the relationship between hAPP, hyperexcitability, and Tau remains unclear. It has previously been established that artificially increasing neuronal activity can accelerate tau pathology[38–40]. However, the expression of hTau has been suggested to strongly dampen circuit excitability[16,41,42] (but see ref. 43). Here we observed that hTau co-expressed with hAPP results in an intermediate circuit excitability level when compared to hAPP or hTau injected alone. Synaptic spread of tau has been shown from the entorhinal cortex to other brain regions[70,71], and most recently this effect has been suggested to occur in human brain via the oligomeric tau species (T22 +)[44]. Remarkably, although hTau co-injection with hAPP somewhat normalized circuit excitability, it also resulted in a significant increase and apparent extracellular translocation of phospho-tau and oligomeric tau species.

The LEC is the first cortical region to undergo end-stage cellular neurodegeneration[1] in AD, specifically, Layer II[2] excitatory cells[4]. Conversely, one of the earliest pathophysiological alterations seen in both humans with AD, and in mouse models of early- and late-onset AD pathology[9,15,16] is altered local circuit excitability[3,72,73]. In agreement with our mechanistic cellular and in vivo findings here, hyperactivity has been shown to preferentially emerge in the LEC region[3]. As with others, our slice electrophysiology assessments of circuit excitability aligned with our in vivo findings as good predictors of hyperexcitability in AD pathology studies[7,14,74]. Our study suggests that hAPP-induced hyperexcitability in the LEC arises not from alterations in the intrinsic or synaptic properties of

https://doi.org/10.1038/s41467-024-52297-3

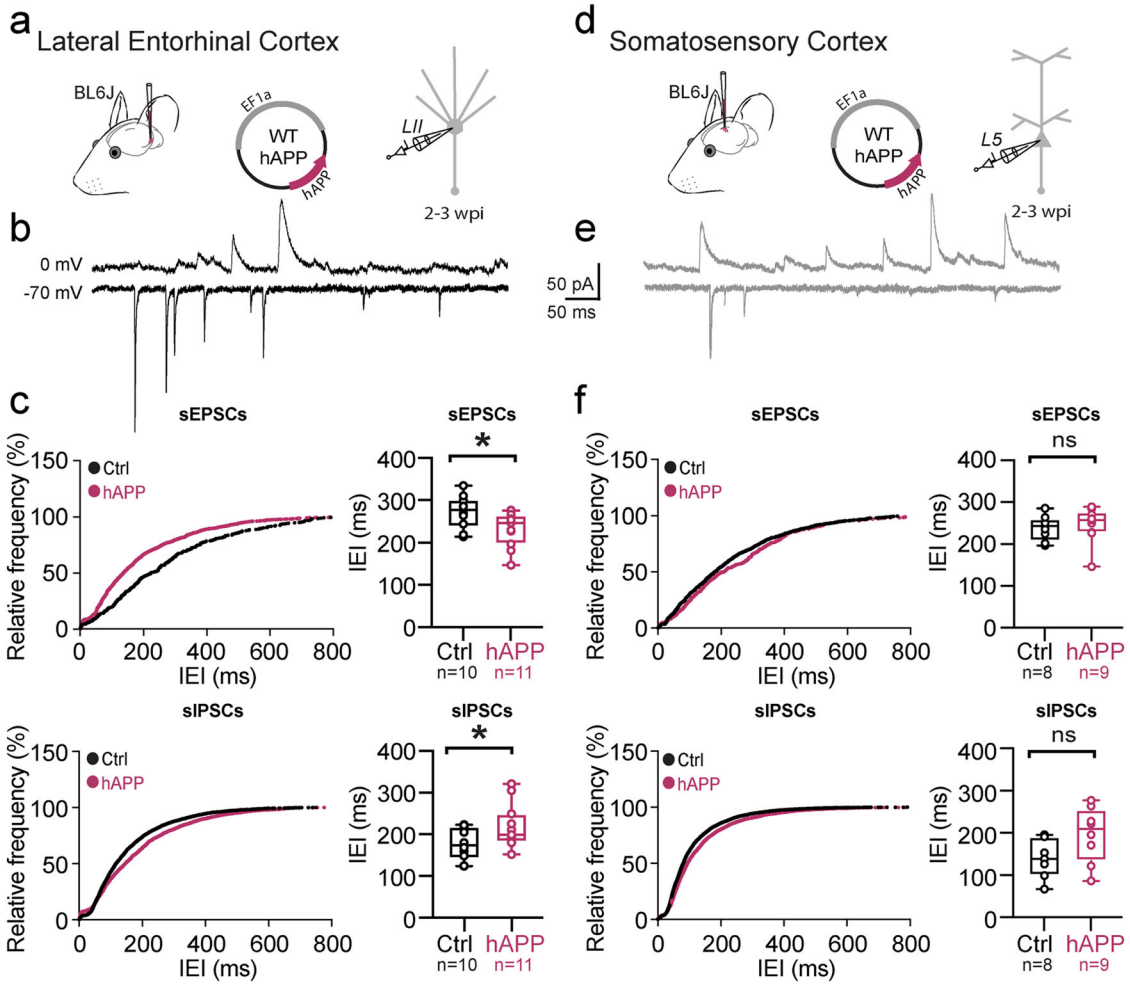

Fig. 5 | Human APP expression induces hyperexcitability in the LEC but not SS Ctx. a Graphical summary of AAV.EF1a.hAPP (or for Ctrl, saline) stereotactic injection in the Lateral Entorhinal Cortex. Excitatory cells were targeted for whole-cell voltage-clamp recordings. **b** Spontaneous events obtained by holding cell voltage at 0 mV (inhibitory post-synaptic currents, IPSCs [top]) and −70 mV (excitatory post-synaptic currents, EPSCs [bottom]), interleaved. **c** Top: Cumulative distribution curve for spontaneous EPSCs in the LEC showing the relationship of relative frequency of events to the inter-event interval (IEI) (left). Quantified averages of IEIs are displayed for each cell as individual data points and compared between Ctrl (black) and hAPP injected (magenta) conditions (right). L2 LEC sEPSCs show a significant reduction in the IEIs (231.7 ± 12.25 ms, 272.7 ± 12.24 ms, hAPP and Ctrl respectively, $p = 0.029$, $t = 2.361$, df = 19, two-tailed unpaired t-test). Ctrl (top) box plot: minimum: 214.5, 25% percentile: 237.7, median: 277.7, 75% percentile: 301.8, maximum: 334.4, range: 120.0; hAPP: minimum: 147.3, 25% percentile: 196.8, median: 247.2, 75% percentile: 264.9, maximum: 276.1, range: 128.8. See Supplementary Fig. 13 for mEPSC data. Bottom: Cumulative distribution curve for spontaneous IPSCs in the LEC showing the relationship of relative frequency of events to the inter-event interval (left). Quantified averages of IEIs are displayed for each cell as individual data points and compared between Ctrl (black) and hAPP injected (magenta) conditions (right). L2 LEC sIPSCs show a significant increase in the IEIs (219.9 ± 15.84 ms, 177.3 ± 12.02 ms, hAPP and Ctrl respectively, $p = 0.047$, $t = 2.097$, df = 19, two-tailed unpaired t-test). Box plot (bottom) Ctrl: minimum: 123.8, 25% percentile: 142.7, median: 174.2, 75% percentile: 218.5, maximum: 223.2, range: 99.44; hAPP: minimum: 152.4, 25% percentile: 182.5, median: 199.5, 75% percentile: 249.3, maximum: 320.9, range: 168.6. See Supplementary Fig. 13 for mIPSC data. **d** Graphical summary of AAV.EF1a.hAPP (or for Ctrl, saline) stereotactic injection in the Somatosensory Cortex. Excitatory cells were targeted for whole-cell voltage-clamp recordings. **e** Spontaneous events obtained by holding cell voltage at 0 mV (IPSCs [top]) and −70 mV (EPSCs [bottom]), interleaved. **f** Top: Cumulative distribution curve for spontaneous EPSCs in the SS Ctx showing the relationship of relative frequency of events to the IEIs (left). Quantified averages of IEI are displayed for each cell as individual data points and compared between Ctrl (black) and hAPP injected (magenta) conditions (right). L5 SS Ctx sEPSCs show no change in the IEIs ($p = 0.7372$, t = 0.3450, df = 15; two-tailed unpaired t-test). Ctrl (top) box plot: minimum: 196.8, 25% percentile: 207.9, median: 243.5, 75% percentile: 260.9, maximum: 285.8, range: 89.01; hAPP: minimum: 146.2, 25% percentile: 227.8, median: 257.5, 75% percentile: 277.8, maximum: 289.2, range: 143.0. See Supplementary Fig. 13 for mEPSC data. Bottom: Cumulative distribution curve for spontaneous IPSCs in the SS Ctx showing the relationship of relative frequency of events to the inter-event interval (left). Quantified averages of IEIs are displayed for each cell as individual data points and compared between Ctrl (black) and hAPP injected (magenta) conditions (right). L5 SS Ctx sIPSCs show no change in the IEIs ($p = 0.0812$, $t = 1.890$, df = 15; two-tailed unpaired t-test). Box plot (bottom) Ctrl: minimum: 66.86, 25% percentile: 99.89, median: 138.2, 75% percentile: 191.3, maximum: 195.5, range: 128.7; hAPP: minimum: 86.38, 25% percentile: 133.9, median: 209.0, 75% percentile: 254.7, maximum: 277.0, range: 190.6. See Supplementary Fig. 13 for mIPSC data. Source data are provided as a Source Data File.

AD-vulnerable LII excitatory cells, but rather from an initial alteration in intrinsic excitability of surrounding interneurons. The fact that short-term hAPP expression in SS cortex caused no changes in PV firing or overall basal circuit excitability supports this notion. Circuit hyperexcitability is likely an influential factor in the early neurodegenerative cascade[75], as it has been shown to exacerbate release of amyloid-beta[76], and also promotes tau pathology and subsequent trans-synaptic tau spread[39] which ultimately tracks with spine synapse degeneration[14] and cell death[77]. Ultimately, regions that first undergo hyperexcitability may also be among the earliest to display these pathological markers as the disease progresses[39,75]. Thus, PV interneurons of the LEC potentially represent a prime

https://doi.org/10.1038/s41467-024-52297-3

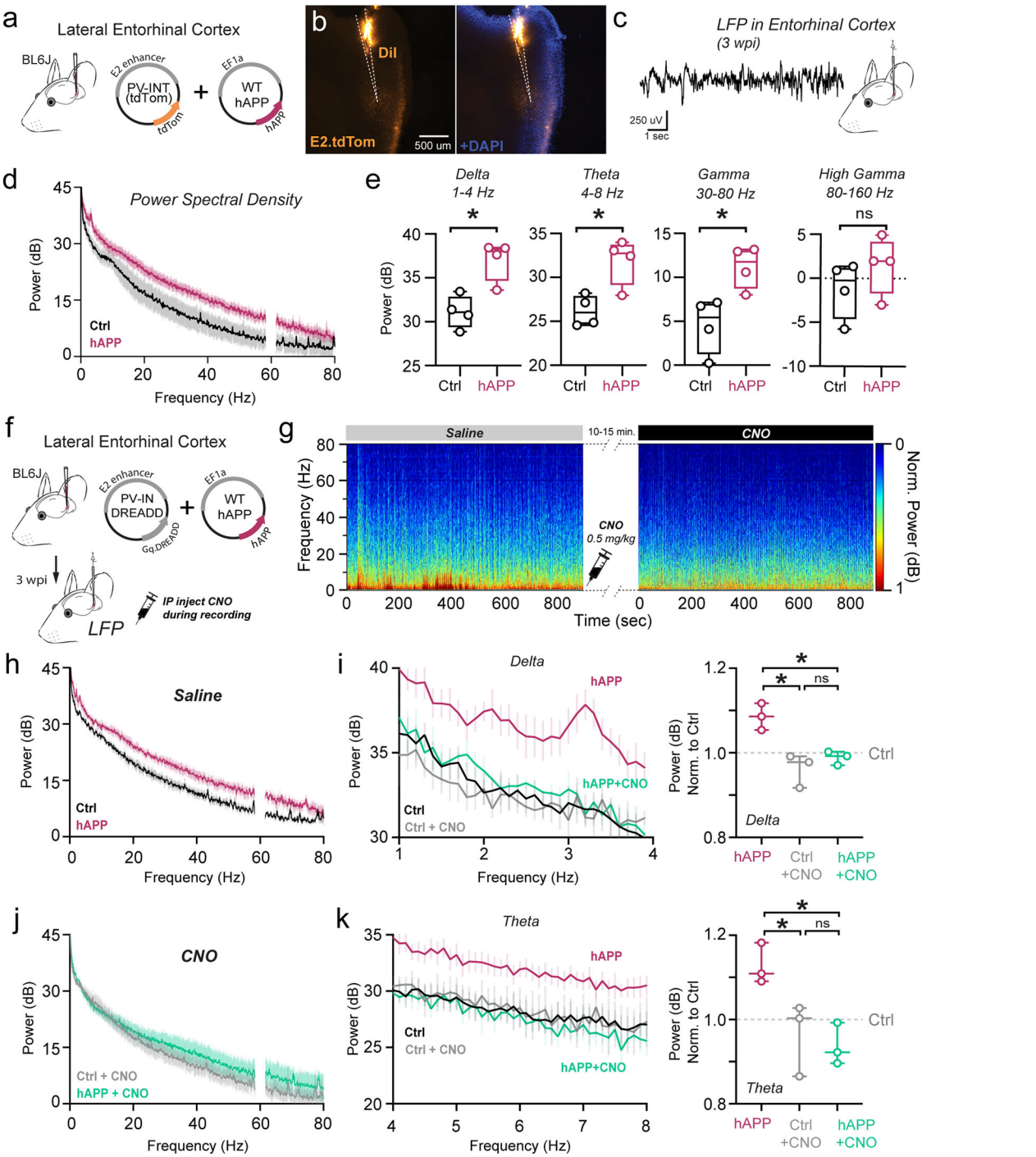

target for therapeutic intervention in the early stages of Alzheimer's Disease.

Methods

Ethics approval and inclusion to participate

All experiments involving animal use were performed in accordance with the ethical guidelines of Emory University Institutional Animal Care and Use Committee (IACUC, PROTO201800199) and ARRIVE guidelines.

Animal husbandry

All animal procedures were approved by the Emory University IACUC. Animal husbandry was performed by the Emory Division of Animal Resources, where animals were kept at room temperature. Mice were housed in ventilated cages (≤5 mice/cage) on a closed-loop auto-water system providing water ad libitum. Dry chow was available ad libitum in each cage.

Acute slice preparation

Acute slices from SS cortex and LEC were prepared from a mixture of 8–12 week old 'wild-type' (C57Bl/6 J) or PV-Cre mice (JAX # 017320, Background: also C57Bl/6 J), evenly dispersed between test and control groups. Male and female mice were used for all experiments with data collected from ≥3 mice per experimental condition. Mice were first fully anesthetized (isoflorane drop method as approved) and then immediately killed by decapitation. The brain was then immediately removed by dissection in ice-cold cutting solution (in mM) 87 NaCl, 25 NaHO3, 2.5 KCl, 1.25 NaH2PO4, 7 MgCl2, 0.5 CaCl2, 10 glucose, and

Fig. 6 | hAPP-induced hyperexcitability observed in vivo can be attenuated by enhancement of PV interneuron excitability. a Graphical summary of AAV.EF1a.hAPP (or for Ctrl, E2.tdTom) stereotactic injection in the Lateral Entorhinal Cortex. **b** 3 weeks post-injection, mice were anesthetized for in vivo glass electrode LFP recordings. **b** is a representative slice at 10x magnification from the LEC where DiI coated electrode recorded from a patch of E2.tdTom+ expressing cells. **c** Raw LFP signal from in vivo glass electrode recordings. **d** Power Spectral Density [PSD] analysis (dark lines: mean, light lines: ±SEM) comparing Ctrl (E2.tdTom+saline injected) to hAPP (E2.tdTom+hAPP injected). **e** Power derived from PSD analysis averaged for each mouse in the Delta (1–4 Hz), Theta (4–12 Hz), Gamma (30–80 Hz), and High Gamma (80–160 Hz) frequency ranges and compared between Ctrl and hAPP. Delta (Ctrl: 31.11 ± 0.94, Min. 28.86, Max. 33.43, Range. 4.57; hAPP: 37.02 ± 1.15, Min. 33.62, Max. 38.43, Range. 4.81; $p = 0.0073$, t = 3.98, df = 6); Theta (Ctrl: 26.20 ± 0.88, Min. 24.57, Max. 28.22, Range. 3.65; hAPP: 31.86 ± 1.34, Min. 27.97, Max. 33.98, Range. 6.01; $p = 0.012$, t = 3.54, df = 6), Gamma (Ctrl: 4.56 ± 1.59, Min. 0.24, Max. 7.13, Range. 6.89; hAPP: 11.17 ± 1.20, Min. 8.01, Max. 13.15, Range. 5.14; $p = 0.016$, $t = 3.32$, df=6), High Gamma (Ctrl: −1.22 ± 1.63, Min. −5.76, Max. 1.35, Range. 7.11; hAPP: 1.49 ± 1.65, Min. −2.98, Max. 4.97, Range. 7.96; $p = 0.2864$, t = 1.170, df = 6). Individual data points (representing biological replicates, $n = 4$ for each group) and box plots are displayed. Statistical significance is denoted as $^*p < 0.05$, as determined by two-tailed unpaired *t*-test. **f** Graphical summary of AAV.E2.Gq.DREADD with AAV.EF1a.hAPP (or for Ctrl DREADD, E2.Gq.DREADD + E2.tdTom) stereotactic injection in the Lateral Entorhinal Cortex. 3 weeks post-injection, mice were anesthetized for in vivo glass electrode LFP recordings with administration of saline or 0.5 mg/kg administration of Clozapine-n-oxide [CNO] during the recording with a wait time after administration of 10–15 min prior to recording. **g** Spectrogram heatmap of LFP power (normalized) from the recording of one mouse after intraperitoneal saline injection (left, 15 min.) and intraperitoneal CNO injection (right, 15 min.). **h** Power Spectral Density analysis (dark lines: mean, light lines: ±SEM) comparing Ctrl DREADD (E2.Gq.DREADD + E2.tdTom + saline) to hAPP DREADD (E2.Gq.DREADD + E2.tdTom + hAPP). **i** [Left] Power Spectral Density analysis only for the Delta frequency range (1-4 Hz) (dark lines: mean, light lines: ±SEM) comparing Ctrl DREADD (black), Ctrl DREADD after CNO (Gray), hAPP DREADD (maroon), and hAPP DREADD after CNO (green). [Right] Power [derived from PSD analysis] averaged for each mouse in the Delta frequency range. (hAPP to Ctrl DREADD + CNO: $p = 0.0063$, hAPP DREADD to hAPP DREADD + CNO: $p = 0.0193$, Ctrl DREADD + CNO to hAPP DREADD + CNO: $p = 0.5758$, df = 7, One-Way ANOVA with Multiple Comparisons) Data represent mean ± SEM, individual data points displayed represent biological replicates, $n = 3$ for each group. **j** Power Spectral Density analysis (dark lines: mean, light lines: ±SEM) comparing Ctrl DREADD after 0.5 mg/kg Clozapine-n-oxide [CNO] injection (E2.Gq.DREADD + E2.tdTom + saline) to hAPP DREADD after 0.5 mg/kg CNO injection (E2.Gq.DREADD + E2.tdTom + hAPP). **k** [Left] Power Spectral Density analysis only for the Theta frequency range (4–10 Hz) (dark lines: mean, light lines: ±SEM) comparing Ctrl DREADD (black), Ctrl DREADD after CNO (Gray), hAPP DREADD (maroon), and hAPP DREADD after CNO (green). [Right] Power [derived from PSD analysis] averaged for each mouse in the Theta frequency range. (hAPP to Ctrl DREADD + CNO: $p = 0.0493$, hAPP DREADD to hAPP DREADD + CNO: $p = 0.0261$, Ctrl DREADD + CNO to hAPP DREADD + CNO: $p = 0.8593$, df = 7, One-Way ANOVA with Multiple Comparisons). Data represent mean ± SEM, individual data points displayed represent biological replicates, $n = 3$ for each group. Also see Supplementary Fig. 14 for related datasets. Source data are provided as a Source Data File.

7 sucrose. Brain slices (250 µm) were sectioned in the sagittal plane using a vibrating blade microtome (VT1200S, Leica Biosystems) in the same solution. Slices were transferred to an incubation chamber and maintained at 34 °C for ~30 min and then at 23-24 °C thereafter. During whole-cell recordings, slices were continuously perfused with (in mM) 128 NaCl, 26.2 NaHO3, 2.5 KCl, 1 NaH2PO4, 1.5 CaCl2, 1.5MgCl2 and 11 glucose, maintained at 30.0 ± 0.5 °C. All solutions were equilibrated and maintained with carbogen gas (95% O2/5% CO2) throughout.

Slice electrophysiology

PV interneurons and excitatory cells were targeted for somatic whole-cell recording in layer 5 region of somatosensory cortex or layer 2 lateral entorhinal cortex by combining gradient-contrast video-microscopy with epifluorescent illumination on custom-built or commercial (Olympus) upright microscopes. Electrophysiological recordings were acquired using Multiclamp 700B amplifiers (Molecular Devices). Signals were filtered at 10 kHz and sampled at 50 kHz with the Digidata 1440B digitizer (Molecular Devices). For whole cell recordings, borosilicate patch pipettes were filled with an intracellular solution containing (in mM) 124 potassium gluconate, 2 KCl, 9 HEPES, 4 MgCl2, 4 NaATP, 3 L-Ascorbic Acid and 0.5 NaGTP. For experiments recording spontaneous and miniature events, an intracellular solution containing (in mM) 120 CsMeSO4, 10 HEPES, 5 TEA.Cl, 4 Na2ATP, 0.5 Na2GTP, 2 MgCl2, 10 L-Ascorbic Acid, and 3 Qx314. To obtain miniature events, slices were perfused with 1 µM TTX for 10 min prior to recording (at least 10 mL run). The same protocol was used for spontaneous and miniature events. In patch experiments using exogenously applied amyloid, slices were incubated in an equal mixture of 0.25 µM $A\beta_{1\text{-}40}$ and $A\beta_{1\text{-}42}$, as described previously[10]. LEC slices were incubated with this solution for 3 h before being transferred to standard extracellular solution for patch recordings. Pipette capacitance was neutralized in all recordings and electrode series resistance compensated using bridge balance in current clamp. Liquid junction potentials were uncorrected. Recordings had a series resistance <20 MΩ. Membrane potentials were maintained near −70 mV during current clamp recordings using constant current bias. Action potential trains were initiated by somatic current injection (300 ms) normalized to the cellular capacitance in each recording measured immediately in voltage clamp after breakthrough[78]. For quantification of individual AP parameters, the 1st AP in a spike train at was analyzed at 12 pA/pF for all cells. Passive properties were determined by averaging the responses of several 100 ms long, −20 pA steps during each recording. Spontaneous and miniature events were recorded at a holding voltage of −70 and 0 mV, one second each, interleaved for 3–5 min. Statistical analyses of spontaneous and miniature events using cell averages, to avoid bias in favor of cells which may receive more inputs or less[74,79]. For regional comparisons of PV interneurons, combined controls from datasets in each region were used. Event detection was carried out using Clampfit (Molecular Devices) using a template matching algorithm and were curated manually with a 4 kHz low-pass filter.

In vivo electrophysiology

Electrophysiological recordings (Local Field Potential) were performed in lightly anesthetized animals (1.0% v/v isoflurane). Pipettes (1–3 MΩ) with a long shank (~ 2 cm) were pulled from borosilicate glass capillaries (1.65 mm O.D, #PG52615-4, Sutter instruments Co., USA) using a vertical puller (Narishige PC-100), coated with Sylgard (DOW), baked in a convection oven at 145 °F for 30 min, and allowed to cool prior to use. The reference electrode (silver chloride) was implanted in the contralateral cerebellum. For recordings, pipettes were filled with sterile saline, coated with DiI, slightly trimmed, and placed onto the silver chloride wire. Positive pressure (52-53.9 mBar) was applied to the pipettes during entry into the cortex and then reduced to <1.0 mBar prior to recording. Recordings were conducted at the same coordinates as the injection site in the LEC (X = ± 3.39; Y = −4.52; α = 0°, Z = −2.0). Electrophysiological recordings were acquired using Multiclamp 700B amplifiers (Molecular Devices). Signals were filtered at 4 kHz (Bessel) and sampled at 10 kHz with the Digidata 1440B digitizer (Molecular Devices). For each session, 3–5 5 min recording sessions were completed. Each animal was first injected intraperitoneally with sterile saline, and after a 15 min wait period were recorded. Subsequently, each animal was injected with 0.5 mg/kg Clozapine N-oxide dihydrochloride (#6329, TOCRIS) reconstituted in sterile saline. Data was analyzed offline. 30 min of recording (total) were analyzed for each mouse: 15 min of saline IP injected condition and 15 min of the CNO injected condition. LFP recordings were subjected to a fast-Fourier transformation (FFT) and converted to Power in decibels using custom code to achieve a power spectral density analysis. Data points

https://doi.org/10.1038/s41467-024-52297-3

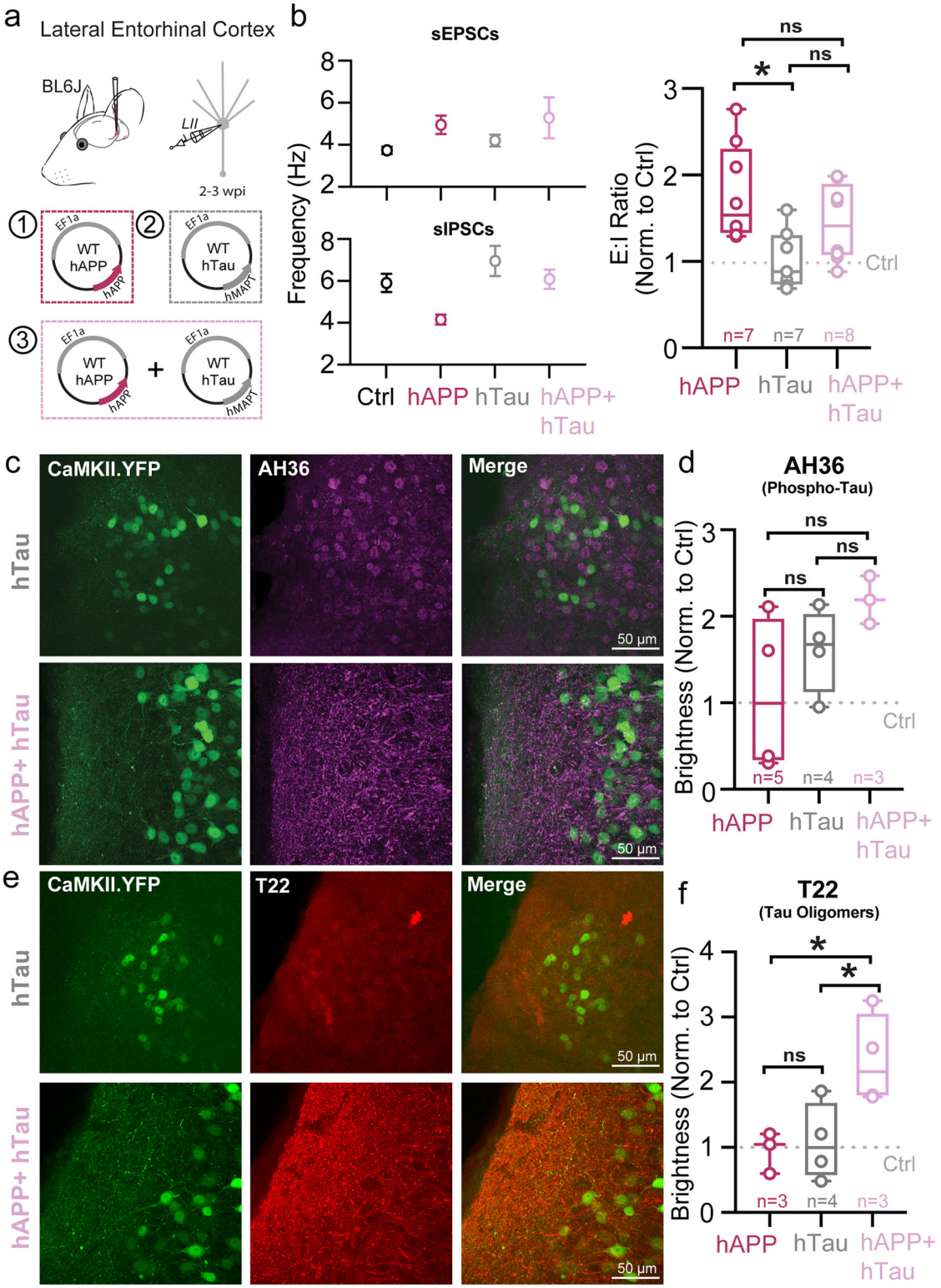

for each frequency range (Delta-High Frequency Oscillations) were averaged for each mouse in each condition to compare for statistical analysis. Statistical analysis was completed using GraphPad Prism. Confirmation of electrode location was completed post-hoc with imaging of LEC sagittal slices on the Nikon Eclipse Ti-E microscope.

Intracranial viral injections

5–9 week old mice were injected with AAV(PHP.eB).E2.tdTom with saline or AAV(PHP.eB).EF1a.hAPP (0.3 µL total, 1:1) in the SBFI vibrissal region of cortex or the Lateral Entorhinal Cortex. For murine APP experiments AAV(PHP.eB).EF1a.hAPP was replaced with AAV(PHP.eB).EF1a.mAPP. For murine APP/hAB chimera experiments, AAV(PHP.eB).EF1a.mAPP/hAB was used. For tau experiments, the four conditions were: Ctrl (CaMKII.eYFP: saline 1:2), hAPP (EF1a.hAPP: CaMKII.eYFP: saline, 1:1:1), hTau (AAV(PHP.eB).EF1a.hMAPT: CaMKII.eYFP: saline, 1:1:1), and hAPP+hTau (EF1a.hAPP: Ef1a.hMAPT: CaMKII.eYFP, 1:1:1). For DREADD experiments, animals were injected with AAV.E2.Gq.DREADD and AAV(PHP.eB).E2.tdTom and either

Fig. 7 | hTau co-expression with hAPP quells hyperexcitability but increases pathological tau. a Graphical summary of AAV.EF1a.hAPP, AAV.EF1a.MAPT (hTau), or co-injected AAV.EF1a.hAPP with AAV.EF1a.MAPT stereotactic injection in the Lateral Entorhinal Cortex. Excitatory cells were targeted for whole-cell voltage-clamp recordings. **b** Spontaneous events obtained by holding cell voltage at −70 mV (excitatory post-synaptic currents, EPSCs [top]) and 0 mV (inhibitory post-synaptic currents, IPSCs [bottom]), interleaved. Quantified averages of event frequency are displayed for each cell normalized to Ctrl values as a ratio of EPSC Frequency to IPSC frequency and compared between hAPP injected (magenta), hTau injected (gray) and hAPP + hTau co-injected (pink) conditions. L2 LEC injected with hAPP showed a significantly elevated E:I ratio compared to hTau injected ($p = 0.0136$, df=20). hAPP and hTau co-injected E:I ratio was not significantly different from hAPP injected ($p = 0.3323$, df = 20) or hTau injected ($p = 0.2175$, df = 20). For all summary graphs, data are expressed as mean (± SEM), data points represent technical replicates (cells). Statistical significance is denoted as $^*p < 0.05$, as determined by an Ordinary one-way ANOVA with Multiple comparisons. Box plot data: hAPP: minimum: 1.292, 25% percentile: 1.315, median: 1.539, 75% percentile: 2.317, maximum: 2.765, range: 1.473; hTau: minimum: 0.6859, 25% percentile: 0.7222, median: 0.8825, 75% percentile: 1.318, maximum: 1.600, range: 0.9138; hAPP + hTau: minimum: 0.8832, 25% percentile: 1.062, median: 1.410, 75% percentile: 1.913, maximum: 1.989, range: 1.105. IHC representative images at 60x magnification for hTau (top) or hAPP+hTau (bottom) injected mice (for Ctrl or hAPP injected, see Supplementary Fig. 15) with staining for either AH36 (**c**) or T22 (**e**). **d** hAPP, hTau, and hAPP+hTau were analyzed for AH36 brightness in the first 100 um of every slice. AH36 brightness was normalized to CaMKII.eYFP brightness to control for any potential variability in viral expression. All groups were then normalized to the Ctrl injected condition. hAPP+hTau showed the highest level of AH36 brightness, although it was not significant over hAPP ($p = 0.1267$) or hTau ($p = 0.4900$) (df = 8, One-Way ANOVA with Multiple Comparisons). hAPP and hTau were also not significantly different ($p = 0.5328$). Box plot data: hAPP: minimum: 0.3056, 25% percentile: 0.3258, median: 0.9949, 75% percentile: 1.986, maximum: 2.113, range: 1.807; hTau: minimum: 0.9517, 25% percentile: 1.112, median: 1.673, 75% percentile: 2.038, maximum: 2.133, range: 1.182; hAPP+hTau: minimum: 1.916, 25% percentile: 1.916, median: 2.193, 75% percentile: 2.469, maximum: 2.469, range: 0.5531. **f** hAPP, hTau, and hAPP+hTau were analyzed for T22 brightness in the first 100 um of every slice. T22 brightness was normalized to CaMKII.eYFP brightness to control for any potential variability in viral expression. All groups were then normalized to the Ctrl injected condition. hAPP+hTau showed a significantly higher level of T22 brightness, above both hAPP ($p = 0.0350$) and hTau ($p = 0.0.0389$) (df = 8, One-Way ANOVA with Multiple Comparisons). hAPP and hTau were not significantly different ($p = 0.9526$). Box plot data: hAPP: minimum: 0.5981, 25% percentile: 0.5981, median: 1.048, 75% percentile: 1.206, maximum: 1.206, range: 0.6079; hTau: minimum: 0.4814, 25% percentile: 0.5575, median: 0.9968, 75% percentile: 1.699, maximum: 1.863, range: 1.382; hAPP+hTau: minimum: 1.776, 25% percentile: 1.782, median: 2.164, 75% percentile: 3.071, maximum: 3.252, range: 1.476. Source data are provided as a Source Data File.

AAV(PHP.eB).EF1a.hAPP or sterile saline (1:1:1). When performing intracranial viral injections, mice were head-fixed in a stereotactic platform (David Kopf Instruments) using ear bars, while under isoflurane anesthesia (1.5–2.0%). Thermoregulation was provided by a heating plate using a rectal thermocouple for biofeedback, thus maintaining core body temperature near 37 °C. Bupivacaine was subcutaneously injected into the scalp to induce local anesthesia. A small incision was opened 5–10 min thereafter and a craniotomy was cut in the skull (<0.5 µm in diameter) to allow access for the glass microinjection pipette. Coordinates (in mm from Bregma) for microinjection in the SS Cortex were X = ± 0.85; Y = −2.5; α = 0°; Z = −0.85, coordinates for the LEC were X = ± 3.39; Y = −4.52; α = 0°, Z = −2.4, −1.5. Viral solution (titer 1×10^{09} to 1×10^{13} vg/mL) was injected slowly (~0.02 µL min-1) by using a Picospritzer (0.3 µL total). After ejection of virus, the micropipette was held in place (5 min) before withdrawal. The scalp was closed with surgical sutures and Vetbond (3 M) tissue adhesive and the animal was allowed to recover under analgesia provided by injection of carprofen and buprenorphine SR. After allowing for onset of expression, animals were sacrificed acute slices were harvested.

Retro-orbital (RO) injection

Male and female mice were given AAV retro-orbital injections as previously described[80]. Mice were anesthetized with 1.8–2% isoflurane. AAV(PHP.eB).E2.Cre.2 A.GFP virus was titrated to 2.4×10^{11} vector genomes total was accompanied by AAV(PHP.eB).Flex.tdTom titrated to 3.1×10^{11} and injected in TurboID+ mice[20] to label PV interneurons throughout cortex. Titrated virus was injected into the retro-orbital sinus of the left eye with a 31 G x 5/16 TW needle on a 3/10 mL insulin syringe. Mice were kept on a heating pad for the duration of the procedure until recovery and then returned to their home cage. After 3 weeks post-injection, mice were provided with biotin water continuously. Biotin water was administered for 2 weeks until acute slice sample collection (total of 5 weeks post-RO injection).

CIBOP studies

PV-CIBOP studies were performed by single retro-orbital injections of AAV(AAV(PHP.eB).E2.Cre.2 A.GFP) as described above to Rosa26-TurboID/wt mice and WT littermate animals at 7 weeks of age, as previously described[21]. Control groups in PV-CIBOP studies also received AAV E2.Cre injections for fair comparisons. After 3 weeks to allow Cre-mediated recombination and TurboID expression, biotinylation (37.5 mg/L in drinking water) was performed for 2 weeks[20]. After 5 weeks (total), acute slices were acquired as described above, with subsequent microdissection of the SS Ctx or the LEC.

Tissue processing for protein-based analysis, including Western Blot (WB)

Tissue processing for proteomic studies, including Mass Spectrometry (MS), were performed similarly to previous CIBOP studies[20,21]. Frozen brain tissues (whole brain homogenate excluding cerebellum for WB and microdissected cortical regions for Fig. 1) either intact or dissected cortex, was weighed and added to 1.5 mL Rino tubes (Next Advance) containing stainless-steel beads (0.9–2 mm in diameter) and six volumes of the tissue weight in urea lysis buffer (8 M urea, 10 mM Tris, 100 mM NaH2PO4, pH 8.5) containing 1X HALT protease inhibitor cocktail without EDTA (78425, ThermoFisher). Tissues were homogenized in a Bullet Blender (Next Advance) twice for 5 min cycles at 4 °C. Tissue were further sonicated consisting of 5 s of active sonication at 20% amplitude with 5 s incubation periods on ice. Homogenates were let sit for 10 min on ice and then centrifuged for 5 min at 12,000 RPM and the supernatants were transferred to a new tube. Protein concentration was determined by BCA assay using Pierce™ BCA Protein Assay Kit (23225, Thermofisher scientific). For WB analyses, 10 µg of protein from brain lysates were used to verify TurboID expression (anti-V5) and biotinylation (streptavidin fluorophore conjugate). Standard WB protocols, as previously published, were followed[20]. All blots were imaged using Odyssey Infrared Imaging System (LI-COR Biosciences) or by ChemiDoc Imaging System (Bio-Rad) and densitometry was performed using ImageJ software.

Enrichment of biotinylated proteins from CIBOP brain

As per CIBOP protocols previously optimized[20], biotinylated proteins were captured by streptavidin magnetic beads (88817; Thermofisher Scientific) in 1.5 mL Eppendorf LoBind tubes using 83uL beads per 1 mg of protein (here 200 µg of protein with 16.6 µL of beads) in a 500 µL RIPA lysis buffer (RLB)(50 mM Tris, 150 mM NaCl, 0.1% SDS, 0.5% sodium deoxycholate, 1% Triton X-100). In brief, the beads 16.6 µL beads were washed twice with 1 ml of RLB and 200 µg of protein were incubated by making up the total volume of the solution up to 500 µl using RPL. After incubation at 4 deg C for 1 h with rotation, beads were serially washed at room temperature (twice with 1 mL RIPA lysis buffer for 8 min, once with 1 mL 1 M KCl for 8 min, once with 1 mL 0.1 M sodium carbonate (Na2CO3) for ~10 s, once with 1 mL 2 M urea in

10 mM Tris-HCl (pH 8.0) for ~10 s, and twice with 1 mL RIPA lysis buffer for 8 min), followed by 1 RIPA lysis buffer wash 4 final PBS washes. Finally, after placing the tubes on the magnetic rack, PBS was removed completely, then the beads were further diluted in 100 µl of PBS. The beads were mixed and 10% of this biotinylated protein coated beads were used for quality control studies to verify enrichment of biotinylated proteins (including WB and silver stain of proteins eluted from the beads). Elution of biotinylated protein was performed by heating the beads in 30 µL of 2X protein loading buffer (1610737; BioRad) supplemented with 2 mM biotin + 20 mM dithiothreitol (DTT) at 95 °C for 10 min. The remaining 90% of sample were stored at −20 °C for western blot or mass spectrometric analysis of biotinylated protein.

Western blotting and Silver Stain

To confirm protein enrichment on the pulldown samples the protein were eluted from the beads as mentioned above and 1/3rd of the eluted protein was resolved on a 4–12% Bris-Tris gel (Invitrogen: cat# NW04125box) and transferred onto iBlot 2 Transfer Stack containing nitrocellulose membrane using the BOLT transfer system. The membranes were washed once with TBS-T (0.1% tween-20) and then blocked with Start Block (37543, Thermofisher Scientific) for 1 h. The membrane was then probed with streptavidin-Alexa-680 diluted in Start Block for 1 h at room temperature. Further, the membranes were washed 3 times and biotinylated proteins were detected on Odyssey Infrared Imaging System (LI-COR Biosciences). In parallel, 2/3rd of the eluted protein samples were resolved on a 4–12% Bris-Tris gel (Invitrogen: cat# NW04125box) and subjected to Silverstein (Pierce™ Silver Stain Kit: Catalog number: 24612) to detect the total amount of protein in each lane according to the manufactured protocol.

Protein digestion, MS, protein identification and quantification

On-bead digestion of proteins (including reduction, alkylation followed by enzymatic digestion by

Trypsin and Lys-C) from SA-enriched pulldown samples (1 mg protein used as input) and

digestion of bulk brain (input) samples (25 µg protein), were performed as previously described with no protocol alterations[20,21]. In brief, after the removal of PBS from remaining 90% of streptavidin beads (10% used for quality control using western blot and silver stain) were resuspended in 90 uL of 50 mM ammonium bicarbonate (NH4HCO3) buffer. Biotinylated proteins were then reduced with 1 mM DTT and further alkylated with 5 mM iodoacetamide (IAA) in the dark for 30 min each on shaker. Proteins were digested overnight with 0.2 µg of lysyl (Lys-C) endopeptidase (127-06621; Wako) at RT on shaker followed by further overnight digestion with 0.4 µg trypsin (90058; ThermoFisher Scientific) at RT on shaker. The resulting peptide solutions were acidified to a final concentration of 1% formic acid (FA) and 0.1% trifluoroacetic acid (TFA), desalted with a HLB columns (Cat#186003908; Waters). The resulting protein solution was dried in a vacuum centrifuge (SpeedVac Vacuum Concentrator). Detailed methods for this protocol have been previously published[20]. Lyophilized peptides were resuspended followed by liquid chromatography and MS (Q-Exactive Plus, Thermo, data dependent acquisition mode) as per previously published protocols[20]. As previously published[81–83], MS raw data files were searched using SEQUEST, integrated into Proteome Discoverer (ThermoFisher Scientific, version 2.5) using the Uniprot 2020 database as reference (91,441 target 37 sequences including V5-TurboID). Raw MS data as well as searched Proteome Discoverer data before and after processing to handle missing values, will be uploaded to the ProteomeXchange Consortium via the PRIDE repository[84]. The false discovery rate (FDR) for peptide spectral matches, proteins, and site decoy fraction were 1 %. Other quantification settings were similar to prior CIBOP studies[20]. Quantitation of proteins was performed using summed peptide abundances given by Proteome Discoverer. We used razor plus unique peptides for protein level quantitation. The Proteome Discoverer output data were uploaded into Perseus (Version 1.6.15) and abundance values were log2 transformed, after which data were filtered so that >50% of samples in a given CIBOP group expected to contain biotinylated proteins, were non-missing values. Protein intensities from SA-enriched pulldown samples (expected to have biotinylated proteins by TurboID) were normalized to sum column intensities prior to comparisons across groups. This was done to account for any variability in level of biotinylation as a result of variable Cre-mediated recombination, TurboID expression and/or biotinylation[20].

Analysis of enrichment of cognitive resilience proteins in regional PV interneuron DEPs

We cross-referenced PV-CIBOP regional proteins ($N = 207$, unadjusted $p < 0.05$) with proteins previously found to be associated with cognitive decline in humans ($N = 55$ proteins associated with cognitive slope in the Religious Orders Study and the Rush Memory and Aging Project (ROSMAP), unadjusted $p < 0.05$)[21,22]. In this prior study, cognitive slope was estimated in the ROSMAP longitudinal study of aging, and cognitive slope was correlated with post-mortem protein abundances, measured by quantitative MS. Proteins that were associated with stable cognitive function (positive association with cognitive slope) were identified as protein markers of cognitive resilience (or pro-resilience proteins). Conversely, proteins ante-correlated with cognitive stability were labeled as anti-resilience proteins. 55 resilience-associated proteins in ROSMAP were identified as regional DEPs in our PV-CIBOP study. The median correlation with cognitive slope for SS Ctx and LEC PV-CIBOP DEPs was estimated and compared across the two regions (two-tailed Mann-Whitney U test).

Integration of PV-CIBOP proteomes with existing human AD proteomic datasets

We cross-referenced our PV-CIBOP regional proteomes with existing human post-mortem proteomes in which the entorhinal cortex (EC), frontal cortex (FC) and other regions were sampled from AD cases (early BRAAK stages I-III, late BRAAK stages IV-VI) and non-AD/non-pathology controls. Proteins were identified as DEPs if they were significantly different comparing AD versus controls within any given region (total of 737 DEPs identified). PV-CIBOP proteins identified by our current study were further assessed for evidence of regional differences within PV interneurons (SS Ctx vs. LEC).

Assessment of human tau/APP protein-protein interactors among PV-CIBOP regional DEPs

We cross-referenced our PV-CIBOP regional proteomic data with human tau protein interactors, previously identified in a meta-analysis across 12 published tau interactome studies[24], in which 2,084 human tau interactors were identified, and among these, 261 were high-confidence interactors if they were identified by at least 3 studies. PV-CIBOP proteins in our study that were also found among these 216 human tau interactors, were further analyzed for evidence of regional differences (SS Ctx vs. LEC) in PV interneurons. The proportions of tau interactors and non-tau interactors across SS Ctx-enriched, LEC-enriched and non-regional PV interneuron proteins were compared (Chi square test).

Using a similar approach, we obtained a list of 243 human APP interactors derived from protein-protein-interaction databases (STRING consortium 2023, Version 12.0, https://string-db.org/) restricting the interactome to physical interactors with medium confidence stringency (confidence scores >0.40, including text mining, experiments and databases). We excluded proteomic studies of extracellular amyloid beta plaques as these are less likely to represent interactions relevant to intra-neuronal APP processing.

RNAscope

RNAscope was performed for confirmation of viral hAPP and mAPP expression, as well as quantification of viral expression in a cell-type-specific manner. RNAscope was performed as instructed by Advanced Cell Diagnostics (ACD). Tissue was prepared from C57Bl/6 J mice (8–12 weeks old), evenly dispersed between test and control groups. Male and female mice were used for all experiments with data collected from ≥3 mice per experimental condition. Mice were injected with AAV(PHP.eB).E2.tdTom and AAV(PHP.eB).hAPP or AAV(PHP.eB).-mAPP (0.3 uL total, 1:1) in one hemisphere and injected contralaterally with AAV(PHP.eB).E2.tdTom and saline (0.3 uL total, 1:1), $n = 3$ each. Hemispheres were randomized. After 2-3 weeks, mice were first anesthetized and then killed by decapitation. The brain was then immediately removed and flash frozen in isopentane on dry ice. Samples were kept at −80 °C prior to sectioning. Tissue was sectioned on a cryostat at 16 µm thickness, mounted onto Superfrost Plus Slides, and stored at −80 °C until use. Samples were fixed and dehydrated according to the RNAscope kit manufacturer (ACDBio) standard protocol. In brief, frozen slides containing tissue sections were immediately dipped in pre-chilled 4% paraformaldehyde (PFA) for 15 min at room temperature. After fixation, slides were briefly rinsed with 1× phosphate buffered saline (PBS) two times to remove excess fixative. Tissue sections were then dehydrated in a series of ethanol solution 50%, 70% and 100% for 5 min at room temperature. After ethanol washes the slides were transferred into a fresh 100% ethanol solution to sit overnight at −20 °C. The following day, slides were taken out of the ethanol solution, air dried for 5 min, and hydrophobic barriers were drawn around each section. The remainder of the RNAscope assay was then performed following the manufacturer's protocol, multiplexing two different probe groups on two different sections from each animal: 1) human APP (catalog #418321), mouse APP (catalog #519001-C2), and CaMKIIα (catalog #445231-C3), or 2) human APP, mouse APP, and Pvalb (catalog #421931-C3).

Immunohistochemistry

Acute slices were acquired as previously described at 100 µm thickness. Immediately following collection from the vibratome, free-floating sections were placed in 4% paraformaldehyde for fixation at room temperature for 1-2 h. Sections were then washed three times in 1x Tris Buffered Saline (1xTBS) for 10 min. To block nonspecific binding, the sections were then incubated with 5% goat serum (in 1xTBS) for 1 h at room temperature. Sections were then incubated overnight at 4 °C on a shaker plate in the primary antibody solution, which contained 0.2% Triton X-100, 1% goat serum, and a 1:1000 dilution of either the AH36 antibody (StressMarq Sciences, #SMC-601) or T22 antibody (Millipore Sigma, #ABN454) in 1xTBS. The next day, sections were washed three times for 10 min in 1xTBS before incubation with the secondary antibody (Alexa Fluor™ 647 at 1:1000; ThermoFisher Scientific, #A-21245) in 1xTBS for 1 h at room temperature on a shaker plate. From the point of secondary antibody incubation, sections were protected from light using aluminum foil. Following secondary antibody incubation, sections were washed again three times for 10 min in 1xTBS, mounted on slides (Fisher Scientific, #1255015), and coverslipped with Fluoromount containing DAPI (ThermoFisher Scientific, #00-4959-52). Slides were then imaged on a Nikon C2 laser-scanning confocal system with an inverted Nikon ECLIPSE Ti2 microscope. Imaging parameters (e.g., laser power, gain) were defined for each primary antibody and were kept consistent between all sections in that primary antibody group.

Image analysis

Images for analysis of RNAscope sections were taken on a Keyence BZ-X800 microscope (KEYENCE; Osaka, Japan) at 40X magnification. Two images were acquired of each mouse LEC hemisphere, and 4 sections were imaged per mouse (total: ~8 images/experiment for an $n = 3$). The acquisition parameters were kept constant throughout imaging of all sections. Four fluorescent channels were used simultaneously; (1) the green channel was assigned for VIVID 520 dye (human APP probe), (2) the blue channel was used for DAPI nuclear stain, (3) the red channel was assigned for VIVID 570 dye (mouse APP probe), and (4) the far-red channel was assigned for VIVID 650 dye (CaMKIIα or Pvalb probes). A z-stack was taken (with 1 µm steps) of each hemisphere, and the full focus feature in the Keyence BZ-X800 analysis software was applied to compress each 10 µm z-stack. These compressed z-stacks were then used for image analysis in HALO v3.6 FISH-IF v2.1.4 (Indica Labs). For immunohistochemistry experiments, 2 sections were imaged per antibody per mouse (total: ~4 images/experiment for an $n = 3$-5). The acquisition parameters were kept constant throughout imaging of all sections. Two channels were used simultaneously; (1) the green channel was assigned for CaMKII.eYFP expression, (2) the red channel was assigned for Alexa Fluor™ 647. For each slice, four line scans of 200 thickness were analyze from the pia to the end of the 60x photo (~180-200 µm total) using ImageJ software. Antibody brightness was normalized to CaMKII.eYFP expression for each condition to control for any slight variation in viral expression. The obtained data was then analyzed for figure generation in Prism (GraphPad). The process from sample fixation to image analysis covered a four-day time frame.

Flow cytometry

Flow cytometry was performed for the confirmation of viral hAPP protein expression. For positive control 5xFAD and their wild-type littermates were used and injected stereotactically in the somatosensory cortex with 1:1 ratio of AAV(PHP.eB).E2.GFP and saline (0.3 µL). While for hAPP expression C57Bl/6 J were also stereotactically injected at a 1:1 ratio with AAV(PHP.eB).E2.GFP and saline or AAV(PHP.eB).hAPP (0.3 µL total). 2-3 weeks after the injections, mice were euthanized (8–10 weeks old) by decapitation and acute slices of 250 µm were obtained and then micro-dissected to isolate the cortical region containing GFP^+ expressing cells using an epi-fluorescent stereoscope (Olympus SZX12). Virus-injected microdisected regions of the brain were then placed into a cutting solution with 0.5 mg/mL protease (P5147–100MG, Sigma-Aldrich) for 60 min with continuous carbogen gas bubbling. Samples were then manually triturated in 300 µL of 1% PBS into a single-cell suspension. Cells were stained with a human-specific APP antibody (SIG-39320, Biolegend). Cells were first fixed in 1x fixation buffer (eBioscience; cat# 00-8222-49) for 30 min on ice, then washed 3x in PBS. Cells were then permeabilized for 30 min using 1x permeabilization buffer (eBioscience; cat# 00-8333-56) on ice.

To determine the presence of hAPP in these cells, fixed and permeabilized cells were incubated with human-specific APP antibody (SIG-39320, Biolegend) at dilution 1:250 for 1 h. cells were then washed with permeabilization buffer 3 times and incubated for 30 min with a secondary antibody at dilution 1:500. Cells were finally washed 3 times with permeabilization buffer, as mentioned above. After the last wash, 250 µl of PBS was added, vortexed and kept on ice in the dark until flow cytometry was performed. Compensation was performed prior to the experiment using a single fluorophore labelled OneComp eBeads™ Compensation Beads (Catalog number: 01-1111-41; Thermofisher).

Statistics, analysis, and reproducibility

Custom Python scripts, Axograph, Graphpad Prism (Graphpad Software), and Excel (Microsoft) were used for analysis with values in text and figures. Statistical differences were deemed significant with α values of $p < 0.05$. All datasets included 3 or more biological replicates. Randomization, blinding, and data exclusion are described in each technique methods subsection. Two-tailed unpaired and paired *t*-tests were used for unmatched and matched parametric datasets, respectively. Where appropriate, group data were compared with 1 or 2-way ANOVA and significance between groups noted in figures was determined with Tukey's or Sidak's multiple post-hoc comparison tests.

Normality was determined using D'Agostino & Pearson omnibus or Shapiro-Wilk tests. For permutation-based false discovery proportion (FDP) estimation, we used permFDP package in R [version 4.3.1], https://github.com/steven-shuken/permFDP for correcting p-values for multiple hypothesis testing. Using a family of unadjusted p values, and 500 permutations, this function returned the corrected rejection threshold to control false discovery (FDR < 5%). For this dataset, the adjusted p-value threshold was 0.0431.

K-means clustering and principal component analysis

K-means clustering and Principal component analysis (PCA) were conducted on datasets from excitatory neurons and PV interneurons, respectively, in the LEC. All passive and active properties were used for each cell to conduct unsupervised clustering. Post-clustering and analysis, Ctrl or hAPP identities were restored to their respective cells.

Analyses of MS data and bioinformatics analyses

Within each MS study, we compared bulk proteomes to SA-enriched proteomes to confirm that expected proteins (from either PV-INTs) were indeed enriched while nonneuronal proteins (e.g. glial proteins) were de-enriched as compared to bulk brain proteomes. We also identified proteins unique to bulk or SA-enriched pulldown samples. Within SA-enriched biotinylated proteins, we restricted our analyses to those proteins that were confidently biotinylated and enriched (based on statistical significance unadj. $P < 0.05$ as well as 2-fold enrichment in biotinylated vs. non-biotinylated samples). This allowed us to exclude proteins that were non-specifically enriched by streptavidin beads. Within biotinylated proteins, group comparisons were performed using a combination of approaches, including differential abundance analysis, hierarchical clustering analysis (Broad Institute, Morpheus, https://software.broadinstitute.org/morpheus), as well as PCA, (in SPSS Ver 26.0 or R). Differential abundance analyses were performed on log2 transformed and normalized abundance values using two-tailed unpaired T-test for 2 groups assuming equal variance across groups or one-way ANOVA + post-hoc Tukey HSD tests for >2 groups). Unadjusted and FDR-corrected comparisons were performed, although we relied on unadjusted p-values along with effect size (fold-enrichment) to improve stringency of analyses. After curating lists of differentially enriched proteins, gene set enrichment analyses (GSEA) were performed (AltAnalyze Ver 2.1.4.3) using all proteins identified across bulk and pulldown proteomes as the reference (background list). Protein-protein interactions between proteins within lists of interest were examined using STRING DB. We also performed GSVA of DEPs identified in bulk as well as PV interneuron proteomes from SS Ctx and LEC to complement GSEA[85,86]. As previously published, statistical differences in enrichment scores for each ontology comparing two groups, were computed by comparing the true differences in means against a null distribution which was obtained by 1000 random permutations of gene labels. Benjamini & Hochberg false discovery rate adjusted p values < 0.05 were considered significant. The reference gene sets for GSVA were the M5 (Mouse) Ontology Gene Sets from MSigDB (https://www.gseamsigdb.org/gsea/msigdb/mouse/collections.jsp?targetSpeciesDB=Mouse#M5).

Reporting summary

Further information on research design is available in the Nature Portfolio Reporting Summary linked to this article.

Data availability

All raw data are available online in repository format, or can be found in the supplementary datasets included here. Additional queries can be referred to the corresponding authors. The PV-interneuron mass spectrometry proteomics data have been deposited to the ProteomeXchange Consortium via the PRIDE partner repository with the dataset identifier PXD053491. The 2020 mouse UniProt database (downloaded from https://www.uniprot.org/help/reference_proteome) was used for searches of mass spectrometry data. Source data are provided with this paper. Project Name: Cortical region confers neuron-type-specific vulnerability to human APP expression. Project accession: PXD053491. Other source data are provided as a Source Data file. Source data are provided with this paper.

References

1. Braak, H. & Braak, E. Neuropathological stageing of Alzheimer-related changes. *Acta Neuropathol.* **82**, 239–259 (1991).
2. Gomez-Isla, T. et al. Profound loss of layer II entorhinal cortex neurons occurs in very mild Alzheimer's disease. *J. Neurosci.* **16**, 4491–4500 (1996).
3. Khan, U. A. et al. Molecular drivers and cortical spread of lateral entorhinal cortex dysfunction in preclinical Alzheimer's disease. *Nat. Neurosci.* **17**, 304–311 (2014).
4. Kobro-Flatmoen, A., Nagelhus, A. & Witter, M. P. Reelin-immunoreactive neurons in entorhinal cortex layer II selectively express intracellular amyloid in early Alzheimer's disease. *Neurobiol. Dis.* **93**, 172–183 (2016).
5. Vossel, K. A. et al. Incidence and impact of subclinical epileptiform activity in Alzheimer's disease. *Ann. Neurol.* **80**, 858–870 (2016).
6. Palop, J. J. et al. Aberrant excitatory neuronal activity and compensatory remodeling of inhibitory hippocampal circuits in mouse models of Alzheimer's disease. *Neuron* **55**, 697–711 (2007).
7. Verret, L. et al. Inhibitory interneuron deficit links altered network activity and cognitive dysfunction in Alzheimer model. *Cell* **149**, 708–721 (2012).
8. Mondragon-Rodriguez, S., Gu, N., Manseau, F. & Williams, S. Alzheimer's Transgenic Model Is Characterized by Very Early Brain Network Alterations and beta-CTF Fragment Accumulation: Reversal by beta-Secretase Inhibition. *Front Cell Neurosci.* **12**, 121 (2018).
9. Petrache, A. L. et al. Aberrant Excitatory-Inhibitory Synaptic Mechanisms in Entorhinal Cortex Microcircuits During the Pathogenesis of Alzheimer's Disease. *Cereb. Cortex* **29**, 1834–1850 (2019).
10. Hijazi, S. et al. Early restoration of parvalbumin interneuron activity prevents memory loss and network hyperexcitability in a mouse model of Alzheimer's disease. *Mol. Psychiatry* **25**, 3380–3398 (2020).
11. Johnson, E. C. B. et al. Behavioral and neural network abnormalities in human APP transgenic mice resemble those of App knock-in mice and are modulated by familial Alzheimer's disease mutations but not by inhibition of BACE1. *Mol. Neurodegener.* **15**, 53 (2020).
12. Zhang, Z. et al. Hyper-excitability of corticothalamic PT neurons in mPFC promotes irritability in the mouse model of Alzheimer's disease. *Cell Rep.* **41**, 111577 (2022).
13. Olah, V. J. et al. Biophysical K(v)3 channel alterations dampen excitability of cortical PV interneurons and contribute to network hyperexcitability in early Alzheimer's. *Elife* **11**, https://doi.org/10.7554/eLife.75316 (2022).
14. Siskova, Z. et al. Dendritic structural degeneration is functionally linked to cellular hyperexcitability in a mouse model of Alzheimer's disease. *Neuron* **84**, 1023–1033 (2014).
15. Nuriel, T. et al. Neuronal hyperactivity due to loss of inhibitory tone in APOE4 mice lacking Alzheimer's disease-like pathology. *Nat. Commun.* **8**, 1464 (2017).
16. Angulo, S. L. et al. Tau and amyloid-related pathologies in the entorhinal cortex have divergent effects in the hippocampal circuit. *Neurobiol. Dis.* **108**, 261–276 (2017).
17. Nilssen, E. S. et al. Inhibitory Connectivity Dominates the Fan Cell Network in Layer II of Lateral Entorhinal Cortex. *J. Neurosci.* **38**, 9712–9727 (2018).

18. Vormstein-Schneider, D. et al. Viral manipulation of functionally distinct interneurons in mice, non-human primates and humans. *Nat. Neurosci.* **23**, 1629–1636 (2020).
19. Titlow, J. S. et al. Systematic analysis of YFP traps reveals common mRNA/protein discordance in neural tissues. *J. Cell Biol.* **222**, https://doi.org/10.1083/jcb.202205129 (2023).
20. Rayaprolu, S. et al. Cell type-specific biotin labeling in vivo resolves regional neuronal and astrocyte proteomic differences in mouse brain. *Nat. Commun.* **13**, 2927 (2022).
21. Kumar, P. et al. Native-state proteomics of Parvalbumin interneurons identifies unique molecular signatures and vulnerabilities to early Alzheimer's pathology. *Nat. Commun.* **15**, 2823 (2024).
22. Yu, L. et al. Cortical Proteins Associated With Cognitive Resilience in Community-Dwelling Older Persons. *JAMA Psychiatry* **77**, 1172–1180 (2020).
23. Mendonca, C. F. et al. Proteomic signatures of brain regions affected by tau pathology in early and late stages of Alzheimer's disease. *Neurobiol. Dis.* **130**, 104509 (2019).
24. Kavanagh, T., Halder, A. & Drummond, E. Tau interactome and RNA binding proteins in neurodegenerative diseases. *Mol. Neurodegener.* **17**, 66 (2022).
25. Chen, C. et al. Early impairment of cortical circuit plasticity and connectivity in the 5XFAD Alzheimer's disease mouse model. *Transl. Psychiatry* **12**, 371 (2022).
26. Koo, E. H. et al. Differential expression of amyloid precursor protein mRNAs in cases of Alzheimer's disease and in aged nonhuman primates. *Neuron* **4**, 97–104 (1990).
27. Matsui, T. et al. Expression of APP pathway mRNAs and proteins in Alzheimer's disease. *Brain Res.* **1161**, 116–123 (2007).
28. Lehmann, L., Lo, A., Knox, K. M. & Barker-Haliski, M. Alzheimer's Disease and Epilepsy: A Perspective on the Opportunities for Overlapping Therapeutic Innovation. *Neurochem Res* **46**, 1895–1912 (2021).
29. Chen, L. et al. Progressive excitability changes in the medial entorhinal cortex in the 3xTg mouse model of Alzheimer's disease pathology. *bioRxiv*, https://doi.org/10.1101/2023.05.30.542838 (2023).
30. Tahvildari, B. & Alonso, A. Morphological and electrophysiological properties of lateral entorhinal cortex layers II and III principal neurons. *J. Comp. Neurol.* **491**, 123–140 (2005).
31. Chen, L., Saito, T., Saido, T. C. & Mody, I. Novel Quantitative Analyses of Spontaneous Synaptic Events in Cortical Pyramidal Cells Reveal Subtle Parvalbumin-Expressing Interneuron Dysfunction in a Knock-In Mouse Model of Alzheimer's Disease. *eNeuro* **5**, https://doi.org/10.1523/ENEURO.0059-18.2018 (2018).
32. Varga, C., Lee, S. Y. & Soltesz, I. Target-selective GABAergic control of entorhinal cortex output. *Nat. Neurosci.* **13**, 822–824 (2010).
33. Gao, R. Interpreting the electrophysiological power spectrum. *J. Neurophysiol.* **115**, 628–630 (2016).
34. Braak, H., Braak, E., Bohl, J. & Bratzke, H. Evolution of Alzheimer's disease related cortical lesions. *J. Neural Transm. Suppl.* **54**, 97–106 (1998).
35. Desikan, R. S. et al. Amyloid-beta-associated clinical decline occurs only in the presence of elevated P-tau. *Arch. Neurol.* **69**, 709–713 (2012).
36. Lue, L. F. et al. Soluble amyloid beta peptide concentration as a predictor of synaptic change in Alzheimer's disease. *Am. J. Pathol.* **155**, 853–862 (1999).
37. Naslund, J. et al. Correlation between elevated levels of amyloid beta-peptide in the brain and cognitive decline. *JAMA* **283**, 1571–1577 (2000).
38. Schultz, M. K. Jr. et al. Pharmacogenetic neuronal stimulation increases human tau pathology and trans-synaptic spread of tau to distal brain regions in mice. *Neurobiol. Dis.* **118**, 161–176 (2018).
39. Wu, J. W. et al. Neuronal activity enhances tau propagation and tau pathology in vivo. *Nat. Neurosci.* **19**, 1085–1092 (2016).
40. Yamada, K. et al. Neuronal activity regulates extracellular tau in vivo. *J. Exp. Med* **211**, 387–393 (2014).
41. Busche, M. A. et al. Tau impairs neural circuits, dominating amyloid-beta effects, in Alzheimer models in vivo. *Nat. Neurosci.* **22**, 57–64 (2019).
42. Minkeviciene, R. et al. Amyloid beta-induced neuronal hyperexcitability triggers progressive epilepsy. *J. Neurosci.* **29**, 3453–3462 (2009).
43. Hall, A. M. et al. Tau-dependent Kv4.2 depletion and dendritic hyperexcitability in a mouse model of Alzheimer's disease. *J. Neurosci.* **35**, 6221–6230 (2015).
44. Colom-Cadena, M. et al. Synaptic oligomeric tau in Alzheimer's disease - A potential culprit in the spread of tau pathology through the brain. *Neuron* **111**, 2170–2183 e2176 (2023).
45. Nassar, M. et al. Diversity and overlap of parvalbumin and somatostatin expressing interneurons in mouse presubiculum. *Front Neural Circuits* **9**, 20 (2015).
46. Munoz-Manchado, A. B. et al. Diversity of Interneurons in the Dorsal Striatum Revealed by Single-Cell RNA Sequencing and PatchSeq. *Cell Rep.* **24**, 2179–2190 e2177 (2018).
47. Ekins, T. G. et al. Emergence of non-canonical parvalbumin-containing interneurons in hippocampus of a murine model of type I lissencephaly. *Elife* **9**, https://doi.org/10.7554/eLife.62373 (2020).
48. Huang, Y. A., Zhou, B., Wernig, M. & Sudhof, T. C. ApoE2, ApoE3, and ApoE4 Differentially Stimulate APP Transcription and Abeta Secretion. *Cell* **168**, 427–441 e421 (2017).
49. Lee, S. I. et al. APOE4-carrying human astrocytes oversupply cholesterol to promote neuronal lipid raft expansion and Abeta generation. *Stem Cell Rep.* **16**, 2128–2137 (2021).
50. Thakur, M. K. & Mani, S. T. Estradiol regulates APP mRNA alternative splicing in the mice brain cortex. *Neurosci. Lett.* **381**, 154–157 (2005).
51. Bjelik, A. et al. Human apoB overexpression and a high-cholesterol diet differently modify the brain APP metabolism in the transgenic mouse model of atherosclerosis. *Neurochem Int* **49**, 393–400 (2006).
52. Bjelik, A. et al. APP mRNA splicing is upregulated in the brain of biglycan transgenic mice. *Neurochem Int* **50**, 1–4 (2007).
53. Dubal, D. B., Broestl, L. & Worden, K. Sex and gonadal hormones in mouse models of Alzheimer's disease: what is relevant to the human condition? *Biol. Sex. Differ.* **3**, 24 (2012).
54. Notkola, I. L. et al. Serum total cholesterol, apolipoprotein E epsilon 4 allele, and Alzheimer's disease. *Neuroepidemiology* **17**, 14–20 (1998).
55. Kivipelto, M. et al. Apolipoprotein E epsilon4 allele, elevated midlife total cholesterol level, and high midlife systolic blood pressure are independent risk factors for late-life Alzheimer disease. *Ann. Intern Med* **137**, 149–155 (2002).
56. Honig, L. S., Kukull, W. & Mayeux, R. Atherosclerosis and AD: analysis of data from the US National Alzheimer's Coordinating Center. *Neurology* **64**, 494–500 (2005).
57. Wang, J. et al. Enhanced Gamma Activity and Cross-Frequency Interaction of Resting-State Electroencephalographic Oscillations in Patients with Alzheimer's Disease. *Front Aging Neurosci.* **9**, 243 (2017).
58. Saito, T. et al. Single App knock-in mouse models of Alzheimer's disease. *Nat. Neurosci.* **17**, 661–663 (2014).
59. Baglietto-Vargas, D. et al. Generation of a humanized Abeta expressing mouse demonstrating aspects of Alzheimer's disease-like pathology. *Nat. Commun.* **12**, 2421 (2021).
60. Mucke, L. et al. High-level neuronal expression of abeta 1-42 in wild-type human amyloid protein precursor transgenic mice:

synaptotoxicity without plaque formation. *J. Neurosci.* **20**, 4050–4058 (2000).
61. Mehr, A. et al. Lack of APP and APLP2 in GABAergic Forebrain Neurons Impairs Synaptic Plasticity and Cognition. *Cereb. Cortex* **30**, 4044–4063 (2020).
62. Yamamoto, K., Yamamoto, R. & Kato, N. Amyloid beta and Amyloid Precursor Protein Synergistically Suppress Large-Conductance Calcium-Activated Potassium Channel in Cortical Neurons. *Front Aging Neurosci.* **13**, 660319 (2021).
63. Agsten, M. et al. BACE1 modulates gating of KCNQ1 (Kv7.1) and cardiac delayed rectifier KCNQ1/KCNE1 (IKs). *J. Mol. Cell Cardiol.* **89**, 335–348 (2015).
64. Lehnert, S. et al. Ion channel regulation by beta-secretase BACE1 - enzymatic and non-enzymatic effects beyond Alzheimer's disease. *Channels (Austin)* **10**, 365–378 (2016).
65. Wong, H. K. et al. beta Subunits of voltage-gated sodium channels are novel substrates of beta-site amyloid precursor protein-cleaving enzyme (BACE1) and gamma-secretase. *J. Biol. Chem.* **280**, 23009–23017 (2005).
66. Manville, R. W. & Abbott, G. W. The Amyloid Precursor Protein C99 Fragment Modulates Voltage-Gated Potassium Channels. *Cell Physiol. Biochem* **55**, 157–170 (2021).
67. Furukawa, K., Barger, S. W., Blalock, E. M. & Mattson, M. P. Activation of K+ channels and suppression of neuronal activity by secreted beta-amyloid-precursor protein. *Nature* **379**, 74–78 (1996).
68. Mayordomo-Cava, J., Yajeya, J., Navarro-Lopez, J. D. & Jimenez-Diaz, L. Amyloid-beta(25-35) Modulates the Expression of GirK and KCNQ Channel Genes in the Hippocampus. *PLoS One* **10**, e0134385 (2015).
69. Sepulveda, F. J., Parodi, J., Peoples, R. W., Opazo, C. & Aguayo, L. G. Synaptotoxicity of Alzheimer beta amyloid can be explained by its membrane perforating property. *PLoS One* **5**, e11820 (2010).
70. Harris, J. A. et al. Human P301L-mutant tau expression in mouse entorhinal-hippocampal network causes tau aggregation and presynaptic pathology but no cognitive deficits. *PLoS One* **7**, e45881 (2012).
71. Pickett, E. K. et al. Spread of tau down neural circuits precedes synapse and neuronal loss in the rTgTauEC mouse model of early Alzheimer's disease. *Synapse* **71**, https://doi.org/10.1002/syn.21965 (2017).
72. Cope, Z. A., Murai, T. & Sukoff Rizzo, S. J. Emerging Electroencephalographic Biomarkers to Improve Preclinical to Clinical Translation in Alzheimer's Disease. *Front Aging Neurosci.* **14**, 805063 (2022).
73. Kelberman, M. A. et al. Age-dependent dysregulation of locus coeruleus firing in a transgenic rat model of Alzheimer's disease. *Neurobiol. Aging* **125**, 98–108 (2023).
74. Caccavano, A. et al. Inhibitory Parvalbumin Basket Cell Activity is Selectively Reduced during Hippocampal Sharp Wave Ripples in a Mouse Model of Familial Alzheimer's Disease. *J. Neurosci.* **40**, 5116–5136 (2020).
75. Rodriguez, G. A., Barrett, G. M., Duff, K. E. & Hussaini, S. A. Chemogenetic attenuation of neuronal activity in the entorhinal cortex reduces Abeta and tau pathology in the hippocampus. *PLoS Biol.* **18**, e3000851 (2020).
76. Bero, A. W. et al. Neuronal activity regulates the regional vulnerability to amyloid-beta deposition. *Nat. Neurosci.* **14**, 750–756 (2011).
77. Olney, J. W. Brain lesions, obesity, and other disturbances in mice treated with monosodium glutamate. *Science* **164**, 719–721 (1969).
78. Taylor, A. L. What we talk about when we talk about capacitance measured with the voltage-clamp step method. *J. Comput Neurosci.* **32**, 167–175 (2012).
79. Pelkey, K. A. et al. Evolutionary conservation of hippocampal mossy fiber synapse properties. *Neuron* **111**, 3802–3818 e3805 (2023).
80. Chan, K. Y. et al. Engineered AAVs for efficient noninvasive gene delivery to the central and peripheral nervous systems. *Nat. Neurosci.* **20**, 1172–1179 (2017).
81. Johnson, E. C. B. et al. Large-scale deep multi-layer analysis of Alzheimer's disease brain reveals strong proteomic disease-related changes not observed at the RNA level. *Nat. Neurosci.* **25**, 213–225 (2022).
82. Rangaraju, S. et al. Quantitative proteomics of acutely-isolated mouse microglia identifies novel immune Alzheimer's disease-related proteins. *Mol. Neurodegener.* **13**, 34 (2018).
83. Rayaprolu, S. et al. Flow-cytometric microglial sorting coupled with quantitative proteomics identifies moesin as a highly-abundant microglial protein with relevance to Alzheimer's disease. *Mol. Neurodegener.* **15**, 28 (2020).
84. Perez-Riverol, Y. et al. The PRIDE database resources in 2022: a hub for mass spectrometry-based proteomics evidences. *Nucleic Acids Res* **50**, D543–D552 (2022).
85. Galea, E. et al. Multi-transcriptomic analysis points to early organelle dysfunction in human astrocytes in Alzheimer's disease. *Neurobiol. Dis.* **166**, 105655 (2022).
86. Hanzelmann, S., Castelo, R. & Guinney, J. GSVA: gene set variation analysis for microarray and RNA-seq data. *BMC Bioinforma.* **14**, 7 (2013).

Acknowledgements

M.J.R.:R56AG072473, RF1AG079269, R21NS133960, Emory ADRC grant 00100569. S.R.: R01 NS114130, RF1 AG071587, R01 AG075820. C.F.: RF1AG079269. N.T.S.: U01AG061357, RF1 AG071587 and R01 AG075820. A.M.G.: F31AG076289. E.B.: F31AG086006. All authors who contributed to the manuscript are included above and have approved the submitted version of this manuscript.

Author contributions

A.M.G. and M.J.R. planned and oversaw all aspects of the study. A.M.G. and M.J.R. wrote the original draft of the paper and received substantial input from S.R. and D.W. S.R. oversaw proteomic data extraction and organization with support from P.K., D.D., N.T.S., and C.C.R. A.M.G. performed or oversaw most of the experiments. K.E.M., E.B., A.M.G., and D.W. led aspects of the study using RNA scope. V.J.O. designed the principal component analysis of physiological features among cell types and provided essential support for LFP data analysis. E.B., A.M.G., and K.S. supported immunofluorescence and confocal imaging work. A.E. supported imaging and validation of in vivo electrode targeting for all in vivo experiments.

Competing interests

The authors declare no competing interests.

Additional information

Supplementary information The online version contains supplementary material available at https://doi.org/10.1038/s41467-024-52297-3.

Correspondence and requests for materials should be addressed to Srikant Rangaraju or Matthew J. M. Rowan.

Peer review information *Nature Communications* thanks Danielle Swaney and the other, anonymous, reviewers for their contribution to the peer review of this work. A peer review file is available.